

# Can atmospheric chemistry deposition schemes reliably simulate stomatal ozone flux-~~(POD<sub>s</sub>)~~ across global land covers and climates?

Tamara Emmerichs<sup>1</sup>, Abdulla Al Mamun<sup>2</sup>, Lisa Emberson<sup>3</sup>, Huiting Mao<sup>4</sup>, Leiming Zhang<sup>2</sup>, Limei Ran<sup>5</sup>, Clara Betancourt<sup>6</sup>, Anthony Wong<sup>7</sup>, Gerbrand Koren<sup>8</sup>, Giacomo Gerosa<sup>9</sup>, Min Huang<sup>10</sup>, Pierluigi Guaita<sup>9</sup>

<sup>1</sup>Institute of Energy and Climate Systems, Troposphere (ICE-3), Forschungszentrum Jülich, Germany, now at Max-Planck-Institute for Meteorology, Germany

<sup>2</sup>Air Quality Research Division, Science and Technology Branch, Environment and Climate Change Canada, Toronto, Ontario M3H 5T4, Canada

<sup>3</sup>Environment & Geography Department, University of York, York, UK.

<sup>4</sup>Department of Chemistry, State University of New York College of Environmental Science and Forestry, Syracuse, NY, 13210, USA

~~<sup>5</sup>Resource Assessment Branch, USDA-NRCS-SSRA-RIAD~~

~~<sup>5</sup>Soil science and Resource Assessment, National Resource Conservation Service, U. S., Department of Agriculture, Raleigh, NC 27609, USA~~

<sup>6</sup>AXA Konzern AG, Cologne, Germany

~~<sup>7</sup>Centre~~<sup>7</sup>Centre for Global Change Science, Massachusetts Institute of Technology, Cambridge, MA, United States of America

<sup>8</sup>Copernicus Institute of Sustainable Development, Utrecht University, Utrecht, the Netherlands

<sup>9</sup>Dep.t of Mathematics and Physics, Catholic University of the Sacred Heart, Brescia, Italy

<sup>10</sup>Earth System Science Interdisciplinary Center, University of Maryland, College Park, MD, USA

Correspondence to: Tamara Emmerichs (tamara.emmerichs@gmx.de)

## Abstract

Over the past few decades, ozone risk assessments for vegetation have ~~been developed~~evolved two methods based on stomatal  $O_3$  flux ~~since this metric is more biologically meaningful than the traditional concentration-based approaches.~~ However, ~~uncertainty remains~~substantial uncertainties remain in the ability to ~~simulate stomatal  $O_3$  fluxes accurately.~~ simulating these fluxes. Here, we investigate stomatal  $O_3$  fluxes ~~simulated by six common air pollution deposition models~~across various land cover types worldwide. ~~simulated by six established deposition models.~~ Hourly  $O_3$  concentration and meteorological data at nine sites were extracted from the Tropospheric Ozone Assessment Report (TOAR) database, a ~~large~~comprehensive global collection of measurements ~~worldwide, provides hourly  $O_3$  concentration and meteorological data which are used to drive the models at 9 sites.~~ for the model simulations. The models estimated ~~summertime~~reasonable  $O_3$  deposition ~~of between~~  $(0.5 - 0.8 \text{ cm s}^{-1}$  ~~in summer), which is~~ mostly in agreement with the literature. Simulations of canopy conductance ( $G_{st}$ ) showed differences ~~between models~~ that varied by land cover type with correlation coefficients of 0.75, 0.80 and 0.85 for forests, crops and grasslands. ~~Climatic conditions, especially among the models. Differences between models were primarily influenced by~~ soil moisture and VPD ~~were also important in determining  $G_{st}$ , vapor pressure deficit, depending upon the model construct. Finally on each model's specific structure.~~ Across models, the range of ~~POD,  $O_3$  damage~~ simulations at each site ~~across models~~ was most ~~in agreement~~consistent for crops (~~36 to 11~~  $\text{mmol } O_3 \text{ m}^{-2}$ ) ~~), followed by~~ forests (~~403 to 2319.5~~  $\text{mmol } O_3 \text{ m}^{-2}$ ) ~~and grasslands (247 to 2633~~  $\text{mmol } O_3 \text{ m}^{-2}$ ). ~~However, when estimating response, crops had the greatest range with differences of up to 35% yield loss for soybeans due to the greater sensitivity of crop flux-response relationships. Nevertheless, ensemble model median response estimates gave results consistent~~ The median estimate across models aligns well with the literature ~~in terms of those at the sites where  $O_3$  damage is most likely vulnerable to occur~~  $O_3$  damage. Overall, this study ~~is an important~~represents a critical first step in developing and evaluating tools for broad-scale assessment of  $O_3$  ~~impact~~impacts on vegetation within the framework of TOAR phase II.

## 1. Introduction

Elevated surface O<sub>3</sub> levels significantly damage vegetation due to the stomatal uptake of O<sub>3</sub> by canopy leaves. Stomatal uptake of O<sub>3</sub> leads to plant tissue injury which in turn causes changes in metabolic functioning, reducing photosynthesis and consequently plant growth and productivity (Mills et al., 2011; Emberson, 2020; Ainsworth et al. 2012; Fuhrer et al., 2016; Grulke and Heath, 2020). Such damage can have significant impacts on crop yields and quality, leading to economic losses and impacting food security in regions already facing scarcity (Avnery et al., 2011; Ainsworth et al. 2017; Ramya et al., 2023). There is an ever-growing body of observational evidence demonstrating a variety of O<sub>3</sub> impacts on different ecosystems (crops, forests, grasslands) in North America, Europe and more recently, Asia (Emberson 2020). Various indices assessing O<sub>3</sub> exposure to vegetation have been developed over recent decades with the stomatal O<sub>3</sub> flux (POD<sub>y</sub>; phytotoxic ozone dose over a threshold y) index found to provide better estimates of O<sub>3</sub> risk to vegetation than the more commonly used concentration-based exposure approaches (e.g., Accumulated Ozone over Threshold (AOT); growing season daylight mean O<sub>3</sub> concentration (M7, M12) (Mills et al., 2011; Avnery et al., 2011). A global overview of spatial distribution and trends using concentration-based metrics was provided in the first Tropospheric Ozone Assessment Report (TOAR) by Mills et al. (2018). During TOAR phase II (TOAR-II), here we conduct a flux-based analysis to ensure the most up-to-date vegetation metrics are provided through this community effort.

O<sub>3</sub> dry deposition to vegetation is in part determined by canopy-level O<sub>3</sub> concentrations. A significant fraction of O<sub>3</sub> uptake occurs through the plant stomata with the remainder depositing on plant cuticular surfaces and the under-storey vegetation and soil. The stomatal contribution can vary between 50 and 80%, depending on the factors controlling the partitioning of stomatal and non-stomatal uptake (e.g., Huang et al., 2022; Wong et al., 2022; Clifton et al., 2023). As such, quantifying canopy stomatal conductance is important for assessing the mass balance of atmospheric O<sub>3</sub> concentrations and its potential damage to vegetation. Both stomatal and non-stomatal processes can vary with environmental conditions such as humidity, solar radiation, temperature and CO<sub>2</sub> concentration as well as vegetation type and density (Clifton et al., 2020a). The occurrence of soil water deficit can also play a crucial role where soil water stress induces stomatal closure (Lin et al., 2020; Huang et al., 2022). There are two commonly used stomatal conductance (g<sub>s</sub>) models - the empirical, multiplicative approach first developed by Jarvis (1976) and the semi-mechanistic coupled net photosynthesis-stomatal conductance models (A<sub>net</sub>-g<sub>s</sub>). The common Jarvis-type models (e.g. Emberson et al., 2000; Ganzeveld et al., 1995; Zhang et al. 2003), widely applied due to their simplicity and computational efficiency, correct a prescribed maximum stomatal conductance with the multiplication of different environmental factors (e.g., temperature, light, soil water and atmospheric moisture). The A<sub>net</sub>-g<sub>s</sub> models couple g<sub>s</sub> to plant photosynthesis by calculating the net

assimilation of CO<sub>2</sub> and estimating g<sub>s</sub> based on the resulting supply and demand of CO<sub>2</sub> (Farquhar et al., 1980; Goudriaan et al., 1985; Ball et al., 1987). A<sub>net</sub>-g<sub>s</sub> models involve multiple non-linear dependencies on soil water, humidity and temperature, among other factors defined by measurement constraints (Ball 1987; Leuning et al., 1997). Heterogeneity of stomatal deposition estimates over different land cover types is anticipated, but model uncertainty depends on the representation of the deposition mechanisms, model parameterisation and meteorological inputs (Hardacre et al., 2015; Clifton et al., 2020b; Huang et al., 2022; Khan et al., 2024).  
Broadly speaking, the pros and cons of these two modelling approaches will tend to depend on the aims of the risk assessment study, the extent of knowledge of the ecosystem being investigated and prevailing bio-climatic conditions. Jarvis-type models are arguably more suitable for studies where less is known about the eco-physiology of the ecosystem since they do not require simulation of net photosynthesis which in itself is inherently difficult to model accurately. However, these models still need to be calibrated for the particular bio-climate of study to ensure temperature and VPD functions are suitable for the prevailing conditions. By contrast, A<sub>net</sub>-g<sub>s</sub> models may be more useful for studies where the physiological response to environmental conditions of the ecosystems is reasonably well understood as they can provide insight into not only pollutant deposition, but also how other environmental conditions in addition to pollution may limit plant growth and productivity more generally.

In this study, the stand-alone version of six O<sub>3</sub> deposition schemes, commonly used in climate or air quality models, are assessed with a focus on their stomatal uptake portion and resulting POD<sub>y</sub> calculation. Using concurrent O<sub>3</sub> concentration and meteorological variable measurement data from the TOAR database enables us to conduct a detailed intercomparison of multiple deposition schemes by avoiding uncertainties arising from using different input data. For this study, various sites have been selected to represent different land cover types and climate regimes around the globe, focusing on sites where observational data are available for O<sub>3</sub> concentration. By assessing the model estimates of stomatal O<sub>3</sub> deposition at these different sites, we aim to identify key differences in model formulation and parameterisation that influence estimates of stomatal O<sub>3</sub> flux and consequent POD<sub>y</sub>. The estimation of the stomatal uptake from water flux measurements taken from the FLUXNET database provides an additional observational constraint as well as an uncertainty estimate at each site.

Furthermore, sensitivity simulations allow us to investigate the variability of stomatal O<sub>3</sub> deposition and plant damage with key input parameters and land cover characteristics. Post hoc, plant damage will be calculated

offline based on the  $POD_y$  simulated by different models and flux-response relationships, where appropriate. Ultimately, we aim to understand the key factors driving stomatal  $O_3$  flux and thus  $POD_y$  and assess the  $O_3$ -induced potential for vegetation damage for different land cover types and global regions.

## 2. Methodology

### 2.1 Meteorological and $O_3$ data from the TOAR-II database

The web version of the  $DO_3SE$  model is coupled to the TOAR database, i.e. the required input data (Table 3) is automatically provided by the database at the respective modelling sites. The TOAR-II database (from now on TOAR) contains harmonised measurements of surface  $O_3$  and its important precursors and key meteorological variables that can impact  $O_3$  concentrations and stomatal  $O_3$  uptake. As one of the largest collections of quality-controlled air pollution measurements in the world, it comprises ground-based station measurements of  $O_3$  concentration at more than 22905 sites globally which cover different periods between 1974 and 2023. These have been collected from different  $O_3$  monitoring networks (e.g., Clean Air Status and Trends Network, CASTNET), harmonised and synthesised to enable uniform processing. The data were selected for inclusion in the TOAR database based on an extended quality control; e.g., sites where the measurement technique changed with time have been excluded. Data errors remain but have been shown to have a minor impact (Schultz et al., 2017). The total uncertainty in modern  $O_3$  measurements is estimated to be  $< 2 \text{ nmol } \mu\text{mol}^{-1}$  (Tarasick et al., 2018). The meteorological data (irradiance, air temperature, relative humidity, precipitation, air pressure, and wind speed) in the database stems from the fifth generation of ECMWF reanalysis (ERA5) for global climate (Hersbach et al., 2020). Data re-initialisation (of precipitation and radiation, Copernicus Climate Change Service, 2017) is bridged by (linear) interpolation. The Leaf Area Index (LAI) data in the database stems from the MODerate resolution Imaging Spectroradiometer (MODIS). TOAR data is freely, and openly available through a graphical user interface and a representational State Transfer interface (<https://toar-data.fz-juelich.de/api/v2/>, last access: 01.11.2024). The TOAR data centre team is committed to the Findability, Accessibility, Interoperability, and Reusability principles (Wilkinson et al., 2016). The centre aims to achieve the highest standards regarding data curation, archival, and re-use (Schröder et al., 2021). In this study, additional meteorological ERA5 data were extracted beforehand and proven for identity. The additionally required by some models

[data \(Table 3\)](#) were extracted from [the TOAR database and](#) the MeteoCloud server (<https://datapub.fz-juelich.de/slcs/meteocloud/index.html>) at Forschungszentrum Jülich.

## 2.2 Observation-constrained stomatal conductance

To compare the modelled stomatal conductance with observational information, we prepared model input data at two sites (Hyytiälä, Harvard Forest) from the FLUXNET 2015 dataset (Pastorello et al., 2020), which is openly available under the CC-BY-4.0 data usage licence. Additional vegetation information for the model input (i.e., LAI, canopy height, and crop calendar data) was provided by the site project investigators. Then, we used the canopy-scale stomatal conductance dataset, SynFlux version 2 to estimate  $G_{st}$  for two forest sites, US-Ha1 and FI-Hyy. While in SynFlux version 1, canopy transpiration is assumed to be equal to total latent heat flux SynFlux version 2 improved its previous estimations (Ducker et al., 2018) by using a machine-learning-based method (Nelson et al., 2018) to partition total evapotranspiration into surface evaporation and canopy transpiration. To train quantile random forest models to relate meteorological conditions with water use efficiency (derived from water and carbon fluxes), periods with minimal surface wetness were chosen during the growing season. These models were then used to back-calculate transpiration for the whole growing season. Instead of the total latent heat flux, the resulting transpiration estimate was used as an input to the inverse Penman-Monteith Equation, reducing the potential high bias in the stomatal conductance estimates in SynFlux version 1.

## 2.3 Summary of sites selected for deposition modelling

Nine sites (Table 1) were selected for this modelling work accounting for the following factors: i. geographical spread, including major continents with terrestrial vegetation; ii. land cover/use types, including the plant functional types (PFTs) which are important in terms of economy, food security, or biodiversity and for which we have fairly good knowledge of  $O_3$  impacts ; iii. availability of meteorological and  $O_3$  data from the TOAR database; iv. availability of observational data describing stomatal conductance of water vapour ( $g_{wv}$ ) estimated from the FLUXNET measurements (Section 2.2); and v. location proximity to previous experiments that have investigated  $O_3$  impacts on vegetation that can help interpret our model results.

167 **Table 1. Sites selected for stomatal deposition modelling using data from the TOAR database grouped by**  
168 **continent. Sites that also have FLUXNET data are denoted by ‘FN’ and those with SynFlux data are**  
169 **denoted by ‘SF’.**

Site (TOAR station id, nearest FLUXNET site id)	Location, station altitude from TOAR	Köppen-Geiger climate classification	Vegetation details (LAI, canopy height in m)	Record (measurement heights in m)	References
Europe					
Hyytiälä, Finland (FI00621, FI-Hyy) FN & SF	61.8611 °N, 24.2833 °E, 104 m	Dfc	LAI: 2.9 Height: 23.3	O <sub>3</sub> : 2014 (4) FLUXNET: 1996/04-2013/09 (14)	Chen et al. (2018); Junninen et al. (2009); Visser et al. (2021)
Grignon, France (FR04038, FR-Gri) FN	48.5819 °N, 1.833 °E, 165 m	Cfb	LAI: 4.3 Height: 3.5	O <sub>3</sub> : 2013/2014 (3) FLUXNET: 2004-2014 (2)	Stella et al. (2013)
Castelporziano, Italy (IT0952A, IT-Cpz)	41.8894 °N, 12.266 °E, 19 m	Csa	LAI: 6.9 Height: 14.0	O <sub>3</sub> : 2013/2014 (19.7) FLUXNET: 2013/2014 (10)	Gerosa et al. (2005, 2009); Fares et al. (2009, 2012); personal communications with Silvano Fares
Asia					
Amberd, Armenia (AM0001R)	40.3844 °N, 44.2605 °E,	BSk (or Dfa)	LAI: 3.9 Height: 1.0	O <sub>3</sub> : 2009/2010	

	2080 m			(3)	
Pha Din, Vietnam (VN0001R)	21.5731 °N, 103.5157 °E, 1466.0 m	Cwa	LAI: 6.9 Height: > 10.0	O <sub>3</sub> : 2015- 2017 (12)	Pieber et al. (2023); Bukowiecki et al. (2018); Yen et al. (2013)
North America					
Quabbin Reservoir/Har vard Forest tower, USA (25-015- 4002, US- Ha1) FN & SF	42.2985 °N, - 72.3341 °E, 312 m	Dfb	LAI: 3.0 Height: 24.0	O <sub>3</sub> : 2010- 2012 (2) FLUXNET: 1993-2012 (24)	Clifton et al. (2019, 2020b); Ducker et al. (2018)
Nebraska, USA (31- 055-0032, US-Ne3)	41.3602 °N, - 96.0250 °E, 400 m	Dfa	LAI: 1.7 Height: 2.5	O <sub>3</sub> : 2010 (2) FLUXNET: 2013/04- (0.5)	Amos et al. (2005); Leung et al (2020)
South America					
Huancayo, Peru (PE0001R)	-12.0402 °N, - 75.3209 °E, 3314 m	Cwb	LAI: 3.6 Height: 1.0	O <sub>3</sub> : 2015 (6)	
Africa					
Mt. Kenya, Kenya (KE0001G)	-0.062 °N, 37.297 °E, 3678.0 m	Aw	LAI: 4.2 Height: 1.0	O <sub>3</sub> : 2015 (unknown)	Henne et al. (2008a,b)



170

171 **Table 2. Land cover type, species and growing season (where SGS = start of growing season and EGS =**  
172 **end of growing season) by site. The equivalent land cover type and soil texture data used by the models**  
173 **used in this study (Section 2.3) are also shown. MESSy does not consider different land cover types.**  
174 **Models that do not consider soil type (i.e. do not include an estimate of soil moisture influence on stomatal**  
175 **deposition) are marked with \*.**

Station site: land cover type (species) and growing season	Web-D- <del>O<sub>3</sub></del> <a href="#">SEDO<sub>3</sub>SE</a>	TEMIR*	NOAH-GEM	ZHANG*	CMAQ
<u>Hyytiälä, Finland:</u> evergreen needleleaf forest (Scots pine) SGS=1, EGS=366	evergreen needleleaf forest, loam	evergreen needleleaf boreal forest	evergreen needleleaf forest, organic material	evergreen needleleaf forest	evergreen needleleaf forest, silty loam (peat)
<u>Grignon, France:</u> crops (rapeseed and wheat) SGS=304, EGS=571	winter wheat, loam	C3 crop	crops/ grassland mosaic, silt loam	crops	crops (wheat), silty loam
<u>Castelporziano, Italy:</u> evergreen broadleaf forest (laurel, abutus, broad-leaved phillyrea, holm oak, pine) SGS=1, EGS=366	evergreen broadleaf forest, loam	Evergreen broadleaf temperate forest	evergreen broadleaf forest, sandy loam	evergreen broadleaf forest	evergreen broadleaf forest, loamy sand
<u>Amberd, Armenia:</u> Grassland, mixed SGS=1, EGS=366	grassland, loam	grassland	grassland, loam	long grassland	grassland, loam
<u>Pha Din, Vietnam:</u> evergreen needleleaf	evergreen needleleaf forest,	evergreen needleleaf	evergreen needleleaf	evergreen needleleaf	evergreen needleleaf

forest SGS=1, EGS=366	loam	temperate forest	forest, clay	forest	forest, clay
<u>Quabbin Reservoir/Harvard Forest tower, USA</u> SGS=93, EGS=312	temperate mixed forest, loam	deciduous broadleaf temperate forest	deciduous broadleaf forest, sandy loam	deciduous broadleaf forest	deciduous broadleaf forest, sandy loam
<u>Nebraska, USA:</u> crops (maize/soybean rotation) SGS=132/148, EGS=278/260	crops (maize, soybean), loam	C3 crop	crops/ grassland mosaic, silty clay loam	crops	crops (corn), silty clay loam
<u>Huancayo, Peru:</u> grassland SGS=1, EGS=366	grassland, loam	grassland	grassland, loam	long grassland	grassland, loam
<u>Mt. Kenya, Kenya:</u> grassland, shrublands SGS=1, EGS=366	grassland, loam	grassland	grassland, loam	long grassland	grassland, silty loam

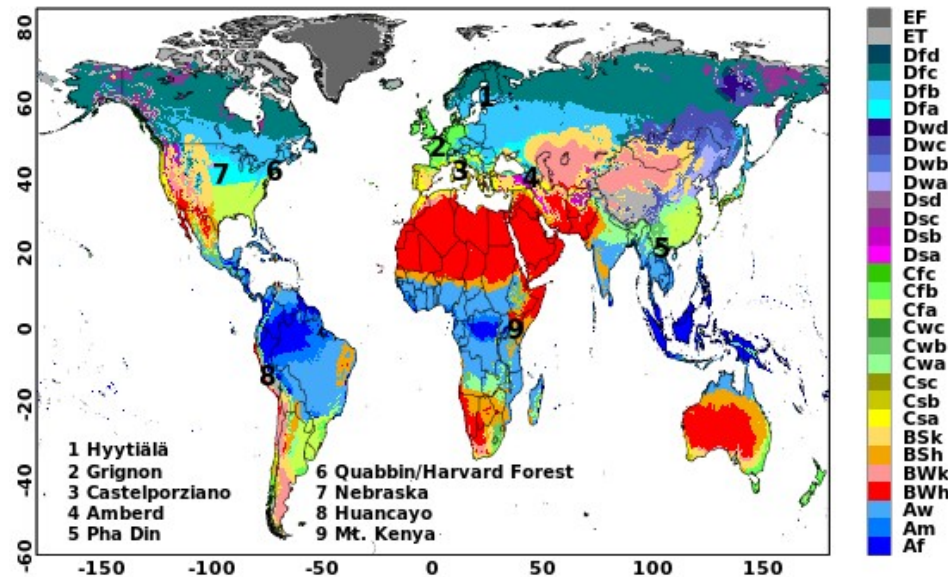
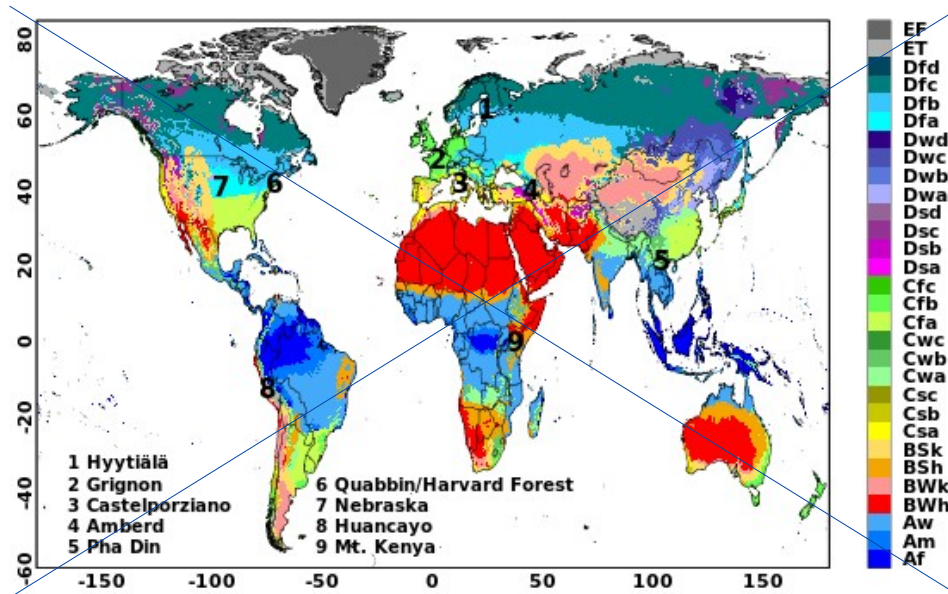



Fig. 1: Locations of 9 selected sites on Köppen-Geiger climate classification map for 1991-2020 (source: Beck et al., 2023). Table 1 specifies the classifications of these sites.


## 2.3 Stomatal deposition models and their key inputs

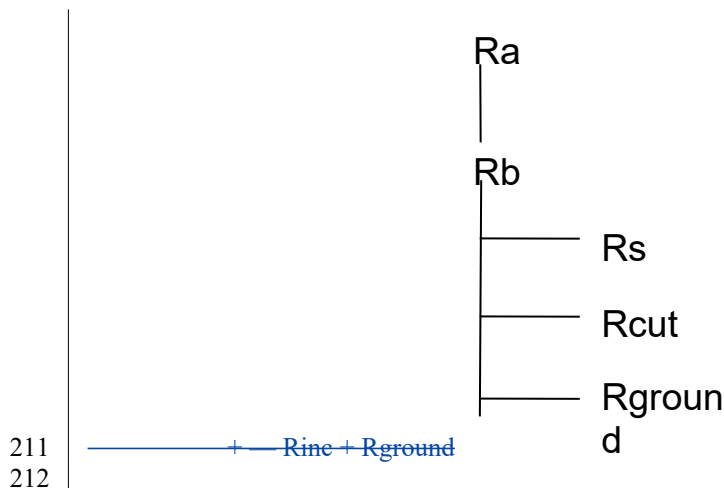
Six widely used empirical/Jarvis and semi-empirical/Ball-Berry types of stomatal deposition models were selected for this study. All of these used models can accommodate a variety of land cover/land use types and provide estimates of stomatal deposition that can be output as both hourly- and season-long cumulative-stomatal deposition metrics. The [key model details/features](#) are described below.

- (1) ~~The empirical/Jarvis-type models~~ ~~–The ZHANG model modifying use~~ a predefined ~~minimum stomatal resistance for sunny and shaded leaves with environmental stress functions in Jarvis-Style (Zhang et al., 2002; 2003; 2006), the Web-DO<sub>3</sub>SE (i.e., a version of DO<sub>3</sub>SE that is directly coupled to the TOAR database) model modifying a predefined maximum stomatal conductance~~ ~~modified~~ with ~~phenology and different~~ environmental ~~stress functions depending on stressors for~~ radiation (PAR), ~~air temperature (T), vapour pressure deficit (VPD) and soil water (SM)~~ ~~– The ZHANG model (Zhang et al., 2002; 2003; 2006) and the Web-DO<sub>3</sub>SE model (i.e., a version of DO<sub>3</sub>SE that is directly coupled to the TOAR database, Emberson et al. 2000) account for sunny and shaded leaves (two-big leaf), the Web-DO<sub>3</sub>SE model also depends on the vegetation phenology, the CMAQ\_J model modifying a minimum stomatal resistance with stress factors for PAR, air temperature (air T) and relative humidity (RH) at leaf surface, and root zone soil moisture (Pleim and Ran, 2011);) and~~ the MESSy model ~~(Ganzeveld et al., 1995; Kerkweg et al., 2006) instead account for one-big leaf~~ CMAQ\_J uses relative humidity (RH) instead of VPD. MESSy calculates the initial stomatal conductance based on the PAR ~~(instead of using a stress function) (Ganzeveld et al., 1995; Kerkweg et al., 2006)~~
- (2) ~~Semi-empirical/Ball-Berry - The CMAQ\_P model~~ ~~using linear regression for C3 and C4 plants based on CO<sub>2</sub> net assimilation (Ran et al., 2017);) and~~ the TEMIR model ~~solves the coupled photosynthesis-stomatal conductance system (Collatz et al., 1991; Farquhar et al., 1980) separately for calculate the stomatal conductance at~~ sunlit and shaded leaves ~~(Tai et al., 2024; Sun et al., 2022) with distinction between C3 and C4 photosynthesis (Collatz et al., 1992), the for C3 and C4 plants depending on net CO<sub>2</sub> assimilation rate, CO<sub>2</sub> partial pressure, atmospheric pressure (Pa) and water vapor pressure for each leave. The~~ NOAA-GEM model ~~involves additionally is different, calculating stomatal conductance at one big leaf using~~ RH instead of VPD (Wu et al., 2011; Niyogi et al., 2009).

All models follow the resistance scheme:

209 |  Reut

210 | i.e.  Rstom



The land cover, growing season, and soil texture specifications used by the models are summarised in Table 2. For crops, we used the GGCM Phase 3 crop calendar (Jägermeyr et al., 2021a) which provides the planting date and maturity day for 18 different crops at a 0.5° land grid cell resolution (Jägermeyr et al., 2021b). For forest trees, we consider four various classes: evergreen-needleleaf (EN), evergreen-broadleaf (EB), deciduous needleleaf (DN), and deciduous broadleaf (DB). For evergreen species, we assume a year-round growing season; for deciduous species, we ~~used~~[use](#) the simple latitude function described in Hayes et al.(2017); and we consider a year-round growing season for tropical species. The soil texture categories used by the models were obtained from the reference studies in Table 1 and the site principal investigators. Table 3 provides the key formulas, input data requirements and references for all models. Key total and stomatal deposition parameters for empirical models ( $g_{\max}$ ) and semi-empirical models ( $V_{C\max}$ ) are described in Table 4, which gives a good indication of the overall difference in the magnitude of stomatal deposition. The models' meteorological and  $O_3$  inputs have been introduced in Section. 2.1.

Table 3. Stomatal deposition models selected for site-scale modelling (list of symbols: Table A1 and Section S3 in the SI, \*uses  $u(h)$ ,  $o3(h)=1$ , for US-Ne:  $u(h)$ ,  $o3(h)=0.3$ ).

Model	Approach	Key Formulas	Key Input data	Reference
ZHANG	Empirical (Jarvis-style)	$G_s(PAR) = \frac{L_{sun}}{r_s(PAR_{sun})} + \frac{L_{shade}}{r_s(PAR_{shade})}$ $r_s = \frac{L_{max}}{L_{max} - L_{min}} \left( \frac{PAR}{PAR_{max}} \right)$	LAI, LUC, Wspeed, ssrd, T2m, Tskin, RH	Zhang et al., 2002; 2003; 2006
Noah-GEM	Semi-empirical, photosynthesis-based (Ball-Berry type)	$R_s = \frac{L_{max}}{L_{max} - L_{min}} \left[ \left( \frac{PAR}{PAR_{max}} \right) \right]$	LAI, LUC, Wspeed, ssrd, strd, T2m, Tskin, RH	Wu et al., 2011; Niyogi et al., 2009
CMAQ_J	Empirical (Jarvis-style)	$G_s(PAR) = \frac{L_{max}}{L_{max} - L_{min}} \left( \frac{PAR}{PAR_{max}} \right)$	LAI, Tair, PAR, ssrd, rn, RH SM	Pleim & Ran 2011



		$\frac{\left( \frac{V_{cmax}}{K_m} \left( \frac{[O_3]}{K_m + [O_3]} \right) \right)}{\left( \frac{[O_3]}{K_m + [O_3]} \right)}$		
MESSy	Empirical (Jarvis-style)	$\frac{V_{cmax} [O_3] / (K_m + [O_3])}{\frac{[O_3]}{K_m + [O_3]} \left( \frac{[O_3]}{K_m + [O_3]} \right) \left( \frac{[O_3]}{K_m + [O_3]} \right)} \left[ \frac{[O_3]}{K_m + [O_3]} \right] \frac{[O_3]}{K_m + [O_3]}$ $r_s(\cdot) \left[ \frac{[O_3]}{K_m + [O_3]} \left( \frac{[O_3]}{K_m + [O_3]} \right) \left( \frac{[O_3]}{K_m + [O_3]} \right) \right]^2$	LAI, ssrd, RH, sw, Tir	Emmerichs et al., 2021; Kerkweg et al., 2006; Ganzeveld et al., 1998
Web-DO <sub>3</sub> SE	Empirical (Jarvis-style)	$r_s = g_{max} \max \{ (([O_3] - [O_3]_{min}) / ([O_3] - [O_3]_{min})) \} \{ (([O_3] - [O_3]_{min}) / ([O_3] - [O_3]_{min})) \}$	Tair, VPD wspeed, P, Pa, O <sub>3</sub> , Gr	Emberson et al., 2000; Bueker et al., 2012; Simpson et al., 2011; Guaita et al., 2023a

**Table 4 Model parameter  $V_{cmax}$  at standardised temperature conditions (25°C) [in  $\mu\text{mol CO}_2 \text{ m}^{-2} \text{ s}^{-1}$ ] and  $g_{max}$  [ $\text{O}_3$  in  $\text{cm s}^{-1}$ ] for the total canopy by land cover/land use type. Note that the values presented in the table were recalculated from the original respective  $r_{smin}$  values for  $\text{H}_2\text{O}$  ( $\text{s m}^{-1}$ ) in ZHANG, MESSy, and CMAQ\_J, and  $V_{cmax}$  values for  $\text{O}_3$  ( $\text{mol O}_3 \text{ m}^{-2} \text{ s}^{-1}$ ) in Web-DO<sub>3</sub>SE .**



Parameter	Web-DO <sub>3</sub> SE	ZHANG	CMAQ_J	TEMIR	NOAH-GEM	CMAQ_P
$G_{\max}$ or $V_{C\max}$	$g_{\max}$ [cm s <sup>-1</sup> ]	$g_{\max}$ [cm s <sup>-1</sup> ]	$g_{\max}$ [cm s <sup>-1</sup> ]	$V_{C\max}^+$ [μmol CO <sub>2</sub> m <sup>-2</sup> s <sup>-1</sup> ]	$V_{C\max}$ [μmol CO <sub>2</sub> m <sup>-2</sup> s <sup>-1</sup> ]	$V_{C\max}$ [μmol CO <sub>2</sub> m <sup>-2</sup> s <sup>-1</sup> ]
Forests	0.44 (EN) 0.49 (EB) 0.55 (DB)	0.25 (EN) 0.42 (EB) 0.42 (DB)  Zhang et al., 2003	0.36 (EN), 0.53 (EB), 0.32 (DB),  Pleim & Ran, 2011	60.1 (EN) 59.0 (EB) 55.4 (DB),  (Oleson et al, 2013; NCAR Technical notes)	57.6 (EN) 96 (EB) 96 (DB)  Niyogi et al., 2009; JAMC	57.6 (EN, Slevin et al 2015), 49.2 (EB, Medi. forest, (EB_tr+E B_te)/2,Oli ver et al., 2022), 55.4 (DB, CLM4.5, Kattge 2009)
Crops	1.1 (wheat) 0.74 (maize) 0.73 (soybean)	0.53	0.91	96.7	76.8	96.7 (CLM4.5)
Grasses	0.66	0.64	0.64	75.1	28.8	75.1 (CLM4.5)

234

235     $POD_y$  is calculated in post-processing, according to the guidelines in UNECE LRTAP (2017):.

$$POD_y = \sum_i \left[ \frac{fst_i}{y} \right] \left( \frac{sun_i}{y} \right) \sum_i \left[ \frac{fst_i}{y} \right] \left( \frac{sun_i}{y} \right) \quad \text{for } fst_i, sun_i \geq y \text{ nmol m}^{-2} \text{ PLA s}^{-1}$$

Where  $fst_i, sun_i$  is the hourly mean  $O_3$  flux in  $\text{nmol } O_3 \text{ m}^{-2} \text{ PLA s}^{-1}$  at sunlit leaves,  $y$  is a species-dependent threshold (crops:  $6 \text{ nmol } O_3 \text{ m}^{-2} \text{ s}^{-1}$ , grassland and forests:  $1 \text{ nmol } O_3 \text{ m}^{-2} \text{ s}^{-1}$ ; UNECE LRTAP (2017) and  $i$  is the number of daylight hours (when  $ssrd > 50 \text{ W m}^{-2}$ ) within the accumulation period (growing season). The term  $(3600/10^6)$  converts from  $\text{nmol m}^{-2} \text{ PLA s}^{-1}$  to  $\text{mmol } O_3 \text{ m}^{-2} \text{ PLA}$ .  $fst, sun$  is calculated by:

$$f_{st, sun} = c \frac{c(z) r_b r_c}{r_b + r_c}$$

Where  $c(z)$  is the  $O_3$  concentration at in  $\text{nmol m}^{-3}$  (calculated from ppb by multiplying by  $P/RT$  where  $P$  is the atmospheric pressure (Pa) and  $T$  is the air temperature (K)

$R$  is the universal gas constant of  $8.31447 \text{ J mol}^{-1} \text{ K}^{-1}$  and  $T$  is the assumed standard air temperature (293 K).

The leaf surface resistance ( $r_c$ ) is given by  $r_c = 1/(g_{st} + g_{ext})$  where  $g_{ext}$  is the inverse of cuticular resistance.

. The leaf boundary resistance is calculated by:

$$r_b = 1.3 \frac{L}{u(h)} \sqrt{\frac{r_b}{L}} \sqrt{\frac{r_b}{L}}$$

Where factor 1.3 accounts for the differences in diffusivity between heat and  $O_3$ ,  $L$  is the crosswind leaf dimension (i.e. leaf width in m) and  $u(h)$  is the wind speed at the top of the canopy.

## 2.4 Description of stomatal deposition model simulations

The result section aims at identifying trends in stomatal deposition models among different land cover types including grass, crops and forests using four model experiments as follows.

In **experiment 1**, the different models are driven by the  $O_3$  and meteorological data from ERA5. We analysed the simulated deposition velocity ( $V_d$ ) split into stomatal and non-stomatal fractions, canopy ( $G_{st}$ ) and sunlit ( $G_{sun}$ ) stomatal conductance.

To include observational constraints, in **experiment 2**, the TEMIR, ZHANG, NOAH, MESSy and CMAQ models were run with data obtained from the FLUXNET database (available for three sites, see Table 1), and the simulated  $G_{st}$  was evaluated with observation-derived values, inferred  $G_{st}$ , of SynFlux. Spearman correlation was applied for the model evaluation, as it can be applied to any datasets including non-parametric and non-linear ones. The US-Ha1 and FI-Hyy sites were considered for the model evaluation due to the availability of SynFlux data at these sites

A sensitivity analysis (**experiment 3**) was performed by driving a set of models with synthetic input data in the following steps: i.  $O_3$  input was perturbed by  $\pm 40\%$  (Sofen et al. 2016). ii. soil water content was perturbed by  $\pm 30\%$  (Li et al., 2020). iii. absolute humidity was perturbed by  $\pm 30\%$ , soil and air temperatures were perturbed by  $\pm 3$ , independently, iv. the growing season, which was mostly approximated by LAI, was shifted by 14 days forward and backward in time. In set (iii) and (iv), relative humidity was calculated from absolute humidity and temperature after their perturbation. In both cases, absolute humidity was capped at the saturation vapour pressure at the corresponding temperature.

Finally, for **experiment 4**,  $g_{max}$  and  $V_{Cmax}$  of the models were varied by  $\pm 20\%$ , based on previous estimates of plant traits dependent uncertainty (e.g., Walker et al., 2017; UNECE LRTAP, 2017).

### 3. Results

#### 3.1 General characteristics of simulated total ~~( $V_d$ )~~ deposition velocity and stomatal ~~deposition~~ contribution

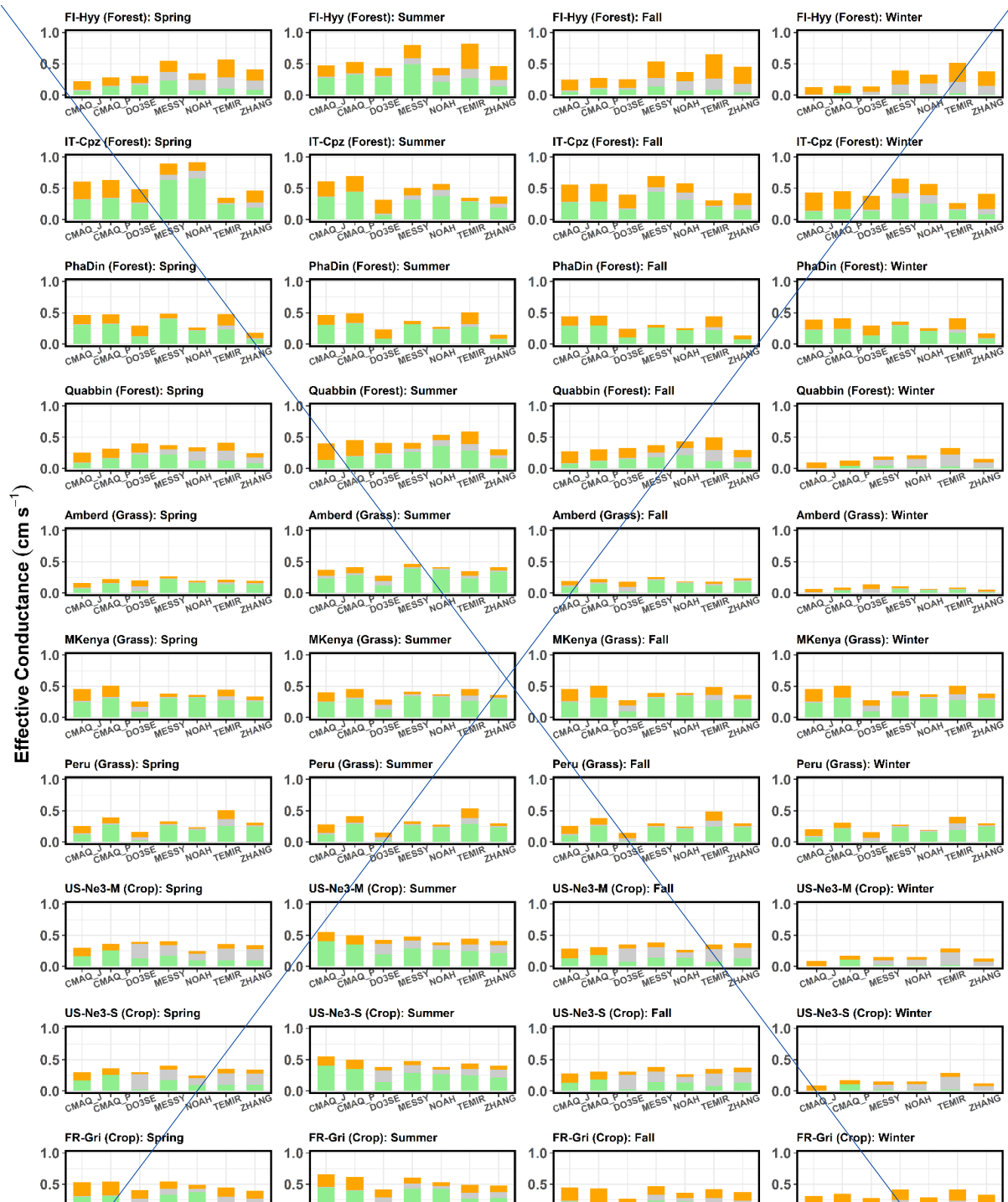
The split of total  $O_3$  deposition between different pathways,  $G_{st}$ ,  $G_{cut}$ ,  $G_{ground}$ , simulated by the 7 models is shown for each of the 9 sites in Figure 2 [and S2](#) (corresponding data are presented in Table S9). This analysis allows us to briefly assess the overall efficacy of the model's ability to simulate [deposition velocity](#)  $V_d$  (by comparisons with previously published values; more complete assessments of model's ability for some of these sites can be found in Clifton et al., 2023) and to compare the importance of the stomatal deposition pathway between models for different land cover types and across different seasons.

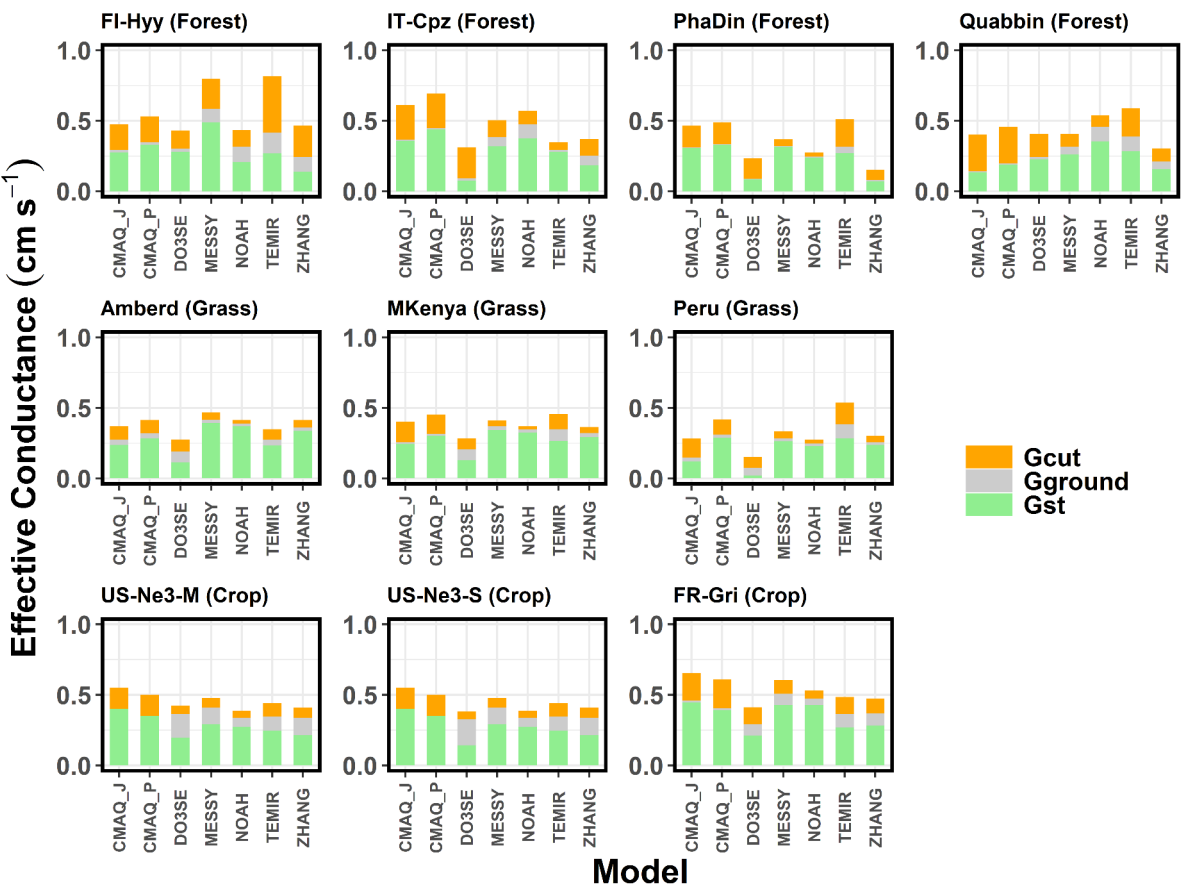
279 Observations of  $V_d$  have only been made at a handful of sites i.e. Hyytiälä, Finland; Castelporziano, Italy;  
 280 Grignon, France and Harvard Forest, US (close to our Quabbin site in terms of proximity, land cover type and  
 281 climate). Overall, the models capture  $V_d$  at these sites compared to observed values reported in previous studies.  
 282 Namely, the observed seasonal cycle in  $V_d$  at Hyytiälä, Finland (needleleaf forest), with lows of  $\sim 0.1 \text{ cm s}^{-1}$   
 283 between January and April and highs of  $0.4 \text{ cm s}^{-1}$  between June to September, averaged over 10 years of  
 284 measurements from Clifton et al. (2023) and Visser et al. (2021) are captured by most models except of MESSy  
 285 and TEMIR, which reach  $V_d$  values of  $0.8 \text{ cm s}^{-1}$  during the summer. Similarly, the strong seasonal cycle in  $V_d$  at  
 286 Quabbin, US (temperate mixed forest), ranging from around  $0.2 \text{ cm s}^{-1}$  between January and April up to  $0.5 \text{ cm}$   
 287  $\text{s}^{-1}$  from June to September in Clifton et al. (2023) is captured by all models. Observed  $V_d$  at Castelporziano,  
 288 Italy (evergreen broadleaf forest) shows relatively constant values throughout the year, commonly between  $0.4$   
 289 and  $0.8 \text{ cm s}^{-1}$  averaged over a 2-year period (Savi & Fares, 2014). The study by Stella et al. (2011) reports  $V_d$   
 290 measurements of  $0.63 \text{ cm s}^{-1}$  (on average) at Grignon (France). At the other sites, no  $\text{O}_3$  dry deposition  
 291 measurement exists and thus we report the observed ranges for the land cover type (and possibly the matching  
 292 climate). Over grassland, Silva and Heald (2018, and references therein) show a mean of 11 measurements of  
 293 daytime  $V_d$  values ( $\sim 0.4 \text{ cm s}^{-1}$ ) in agreement with our models. Measurements exist at soybeans and maize crops  
 294 which indicate  $V_d$  values of  $0.7$  (Meyers et al., 1995) and  $0.4 - 0.6 \text{ cm s}^{-1}$  (Stella et al., 2011), respectively. Thus,  
 295 the models seem to estimate too low deposition at soybeans.  
 296 In terms of deposition pathways, for all sites and models, stomatal deposition consistently ranks as the most  
 297 important pathway in the summer, whereas in winter and, for some models, in the fall  $G_{st}$  decreases to zero to  
 298 very low at sites with seasonal variation in vegetation coverage. The importance of the pathway varies with land  
 299 cover type and season. The highest stomatal contribution of 90 % (NOAH model) is shown at the Amberd site.  
 300 Among the different land cover types, the highest average stomatal contribution to deposition during the summer  
 301 is estimated across grass (67 %), followed by crops (65 %) and forests (59 %). The seasonal importance of  
 302 stomatal contribution is not seen for the tropical sites as the year- round growing season means that stomatal  
 303 conductance is driven by solar radiation which is constant throughout the year (e.g. Hardacre et al., 2015).  
 304 Previous studies involving measurements and partitioning approaches (Horvath et al., 2018, Meszaros et al.,  
 305 2009) indicate that the non-stomatal  $\text{O}_3$  deposition pathways (i.e.,  $G_{\text{ground}}$  and  $G_{\text{cut}}$ ) are very strong (in some cases,  
 306 dominant over  $G_{st}$ ) at short vegetation such as the grasslands. Despite there are multiple factors such as wind  
 307 speed, solar radiation, LAI, etc., that control the relative contributions of the three deposition branches,  $G_{st}$  is the  
 308 dominant pathway at the three grassland sites of the current study (Amberd, Mt Kenya, and Peru). At the  
 309 Amberd and [PeruPeru](#) sites,  $G_{\text{cut}}$  and  $G_{\text{ground}}$  are [small since low dewind speed reduces downward mixing of](#)

ozone to lower wind speeds (e.g., the surface (atmospheric resistance, e.g., at the Peru Site in the Summer season, the mean wind speed was  $1.0 \text{ cm s}^{-1}$  and the  $G_{\text{cut}}$  and  $G_{\text{ground}}$  contributions in the TEMIR model were 21 % and 12 %, respectively; Table S3).

In contrast, at the Mt Kenya site,  $G_{\text{st}}$  overcomes the exceeds  $G_{\text{cut}}$  and  $G_{\text{ground}}$  due to higher, since the strong solar radiation at this site (annual mean is  $246 \text{ W m}^{-2}$ , Table S2-) at this site favours stomatal opening. Besides that, LAI is a very important governing factor for  $G_{\text{st}}$ . Therefore, it can be inferred that the  $\text{O}_3$  deposition pathway depends on not only the land cover type but also meteorological drivers. The relative contributions of each deposition pathway depends on the interplay between these key factors at a particular site. Among the models, Web-DO<sub>3</sub>SE estimated the lowest stomatal contribution at grass (Fig. 2) most likely due to its parallel pathways to cuticle, soil and stomata, with the former scaled by LAI with a constant cuticular deposition of  $2500 \text{ s m}^{-1}$ . Such differences in model structures likely led to the wide-ranging partitioning. For example, for the Quabbin site (summer), all models simulate  $G_{\text{cut}}$  ranging from 15-65 %,  $G_{\text{ground}}$  from 2-19 % and  $G_{\text{st}}$  from 33-66 % despite their agreement on the overall  $V_d$  values (total bar). Models agree better in the partitioning of  $\text{O}_3$  dry deposition to crops with summer stomatal fraction contributions ranging between 46-73 %, 37-73 % and 51-81 % for US-Ne3 Maize, US-Ne3 soybeans and FR-Gri (rapeseed and wheat). Most models estimate non-stomatal deposition equal to or larger than the stomatal contribution to deposition outside of the tropics in winter and fall, and to some extent in spring. This again emphasises the importance of the stomatal contribution to the seasonal cycle of total deposition as also found in Clifton et al. (2023). Similarly, as seen at grasslands, Web-DO<sub>3</sub>SE (Fig. 2, Table S3) accounts for the highest non-stomatal deposition at crop sites.

Across all forest sites, models show significant cuticular uptake throughout the year ranging between 11 % and 94 % contribution. At FI-Hyy,  $G_{\text{cut}}$  averages ~50 % across all seasons and all models with higher estimates of ~55 % by the TEMIR model due to the higher wind speed at FI-Hyy (annual mean wind speed is  $3.2 \text{ m s}^{-1}$ ; Table S2) favoring cuticular deposition as suggested by Rannik et al. (2012). At IT-Cpz, our models estimate on average around 43 % (20-80 %) to be non-stomatal deposition, close to the previously reported ranges (Gerosa et al. 2005, Fares et al. 2012, Fares et al. 2014), which were up to 57 % from non-stomatal deposition and 30-60 % from stomatal uptake. A similar partitioning (59 %  $G_{\text{st}}$ , 33 %  $G_{\text{cut}}$ , 5 %  $G_{\text{ground}}$  model average in summer) is seen at PhaDin.





339

340 **Fig. 2** Seasonal Mean effective conductances of the cuticular ( $G_{\text{cut}}$ ), ground ( $G_{\text{ground}}$ ), and  
341 stomatal ( $G_{\text{st}}$ ) deposition pathways of  $\text{O}_3$  across various models and sites (Exp#1) during the summer  
342 season (US-Ne3-S=soybeans, US-Ne3-M=maize). Respective figures for the other seasons are presented in  
343 the supplement.

344

345 All models except Web-DO<sub>3</sub> SE were compared on a seasonal and hourly basis with the SynFlux  $G_{\text{st}}$  data for US-  
346 Ha1 and FI-Hyy sites (Figures S2, S3). CMAQ\_J, NOAH, TEMIR, and ZHANG show reasonable agreement at

the Quabbin forest (US-Ha1) whereas CMAQ\_P and MESSy show quite significant overestimates at both FI-Hyy and Harvard Forest (Table S4S5) and CMAQ\_J overestimates at FI-Hyy only. Note that NOAH and ZHANG show significant underestimates at FI-Hyy while agreeing well with SynFlux at Harvard Forest (Quabbin). The underestimates by the ZHANG model are consistent with the results from a similar comparison for Yellowstone National Park in the US by Mao et al. (2024). Compared to Harvard Forest, FI-Hyy is the most humid and cloudy with the lowest solar radiation flux, and these conditions likely contribute to the underestimates by the NOAH and the ZHANG model as identified by Mao et al. (2024). The differences between modelled and SynFlux  $G_{st}$  do not seem to be associated with the model types, i.e. empirical or photosynthesis-based models.

The correlation of the diurnal cycle of  $G_{st}$  calculated by the models with the inferred  $G_{st}$  by SynFlux for US-Ha1 and FI-Hyy (Fig. S4) confirms that models generally capture the temporal patterns of  $G_{st}$  of at least these two different forest types and climates (FI-Hyy: EN, temperate, subarctic; Quabbin: DB, moist temperate). The best Spearman correlations are found at FI-Hyy and range between 0.73 by the MESSy model and 0.85 by the TEMIR model. Overall lower correlations are found at the Quabbin site ranging from 0.65 for the NOAH and MESSy models to 0.82 for the CMAQ\_P model. This poorer correlation suggests that additional water stress may limit stomatal conductance at Quabbin, which the models do not capture, compared to FI-Hyy. Notably, a similar range of correlation coefficients (0.61 – 0.93) was found when modelled  $G_{st}$  values obtained using the TOAR input data were compared with SynFlux  $G_{st}$ . As SynFlux data were generated using FLUXNET measurement data, this result corroborates the validity of using the TOAR database as input to Web-DO<sub>3</sub>SE, developed as a service website to aid in risk assessment of O<sub>3</sub> damage to European vegetation.

To identify the key drivers of the  $G_{st}$  model schemes among different land cover types and climate conditions, we also compare estimates of  $G_{st}$  between models for all sites and analyse the similarity of  $G_{st}$  diurnal cycles in empirical and photosynthesis models. [Here, it is important to understand the model distinction between shaded and sunlit leaf \( \$G\_{sun}\$ , Fig 4\).](#) The average diurnal variations of stomatal conductance ( $G_{st}$ ) of O<sub>3</sub> at the 9 sites for each season are shown in Figure 3 and S7. This also helps interpret the modelled stomatal conductance of sunlit leaves ( $G_{sun}$ ) shown in Fig 4 and S8. Across all models, the diurnal mean  $G_{st}$  (Fig. 3) varied from 0.15 cm s<sup>-1</sup> (Quabbin) to 0.50 cm s<sup>-1</sup> (Mt. Kenya). In the TEMIR and the ZHANG model, roughly 50% of  $G_{st}$  occurs at the sunlit part of the leaves. Web-DO<sub>3</sub>SE and CMAQ\_P  $G_{sun}$  contribute 30 % on average (Fig. 4). At mid-to-high latitudes, the model spread is limited to the summer season, whereas at tropical sites, it is similar throughout the

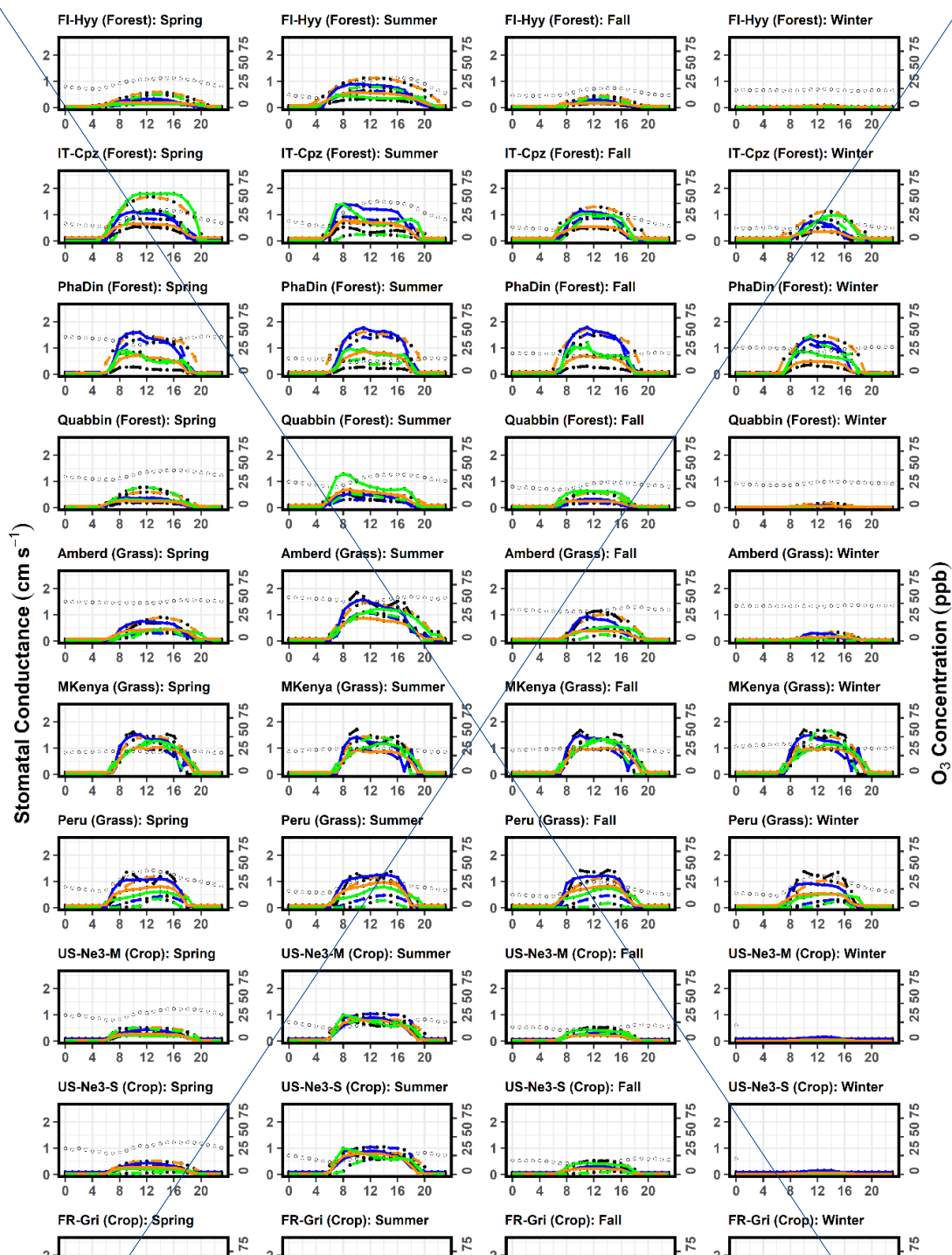


year. During the day, models show a spread of  $1.2 \text{ cm s}^{-1}$  in  $G_{st}$  at the forest and grassland sites during the summer while their predictions agree most at the crop sites (throughout the year) with a maximum of  $1.0 \text{ cm s}^{-1}$ . This is due to the flux response relationship which has a more sensitive response (steeper slope for most crops) due to a higher threshold (see Table 5 for the equations describing the steepness of the change). Results among the same model type differed significantly while different model types could produce similar results at the same location. For the sites with distinct seasonal variations, model differences were the largest in summer.

In comparison, TEMIR and ZHANG, photosynthesis-based and Jarvis-style, respectively, are both governed mainly by solar radiation (see higher  $G_{sun}$  in Fig. 4), showing close agreement, except in summer, at the forest sites (ZHANG values are very low). Only these two show a midday depression in  $G_{sun}$  at the peak of solar radiation at Mt Kenya (the site with the highest radiation). The ZHANG model also estimated this feature for  $G_{sun}$  and  $G_{st}$  at other grassland sites (Fig. 3 and 4). This feature could be due to the day length (seasonality) scaling of  $V_{Cmax}$  in TEMIR, causing  $G_{st}$  to increase significantly during summer at higher latitude sites. In contrast, at lower latitude sites (Mt Kenya and Huancayo, Peru), the seasonal variation in day length is smaller and subsequently smaller seasonality in  $V_{Cmax}$  and  $G_{st}$ . The TEMIR and the CMAQ\_P models, both photosynthesis-based, estimate very similar  $G_{sun}$  values (Fig. 4) at PhaDin (fall, winter), IT-Cpz (spring, summer) and FI-Hyy (summer) whereas the  $G_{st}$  estimates show significant differences. The opposite occurs at Quabbin where the  $G_{sun}$  values of the two models differ much more than the  $G_{st}$  estimates. These results illustrate that the different fractionations between shaded and sunlit leaves could mainly contribute to the model spread in stomatal conductance.

Further examination of individual models' features can shed light on the causes of model/site differences in  $G_{st}$ . The MESSy  $G_{st}$  value is strongly governed by LAI followed by soil moisture, and in all other respects MESSy treats different land cover types the same. Therefore, MESSy simulates the highest  $G_{st}$  values at PhaDin, Grignon and Mt. Kenya with LAI values of 6.9, 4.3 and  $4.2 \text{ m}^2 \text{ m}^{-2}$ , respectively (Table 1). In contrast to PhaDin, the high LAI site IT-Cpz ( $6.9 \text{ m}^2 \text{ m}^{-2}$ ) experiences significant water stress during summer. This is only captured by MESSy and NOAH indicating higher sensitivity to water stress. During the day, an evident midday depression of  $G_{st}$  due to hot weather and water shortage is seen accompanied by a peak in the early morning evident from NOAH, same as has been observed in Mediterranean ecosystems (e.g. Gerosa et al. 2005). The NOAH model accounts for the direct effect of relative humidity on  $G_{st}$  (see model description in the supplement) and subsequently modelled a depression in  $G_{st}$  at the daily onset (8 am). This variation explains the  $G_{st}$  peak at

405 IT-Cpz and Quabbin, which are especially in the summer the two driest among all sites. Due to the dry  
 406 conditions at the Quabbin site, low soil water and relative humidity, most models, except NOAH, simulate the  
 407 lowest summer daily mean  $G_{st}$  values among all sites. The high estimate by the NOAH model can be explained  
 408 by the highest  $V_{Cmax}$  value among the photosynthesis models (Table 4). The high  $g_{max}$  value of  $0.55 \text{ cm s}^{-1}$  used in  
 409 Web-DO<sub>3</sub>SE leading to large estimates is largely dampened by strong soil moisture stress at IT-Cpz (Table S2).  
 410 Similarly, Web-DO<sub>3</sub>SE estimates the lowest  $G_{st}$  (among the models) values at the Peru site (grassland) due to a  
 411 strong limitation by the  $f_{temp}$  function on stomatal conductance suggesting that the minimum temperature for  
 412 stomatal opening at  $12^\circ\text{C}$  is too low for these cool temperate conditions. The ZHANG estimates are generally  
 413 governed by  $g_{max}$ , explaining the highest and lowest  $G_{st}$  values of all models simulated with the ZHANG model  
 414 at grassland and forest sites, respectively. The CMAQ\_J model has the lowest  $g_{max}$  values, but it is strongly  
 415 impacted by soil moisture. The additional dependence of the ZHANG model on solar radiation is reflected in  
 416 higher  $G_{sun}$  relative to  $G_{st}$  (Fig. 3 and 4). TEMIR also simulates the smallest spread of  $G_{st}$  among the 3 grassland  
 417 sites (Ambred, MKenya, Peru), as temperature acclimation of photosynthesis (Kattage and Knorr, 2007) is  
 418 implemented. The different temperatures among the 3 sites have smaller effects on photosynthetic capacity and  
 419  $G_{st}$  than other models. Despite explicitly considering soil water stress, TEMIR does not capture the impacts of  
 420 water stress on  $G_{st}$  in IT-Cpz and Quabbin in the summer, as the equivalent soil moisture threshold to trigger soil  
 421 water stress at IT-Cpz and Quabbin is very low ( $<0.1 \text{ m}^3 \text{ m}^{-3}$ ). Both versions of CMAQ respond very strongly to  
 422 soil moisture which may not be accurate for each site. The differences between CMAQ-J and CMAQ-P are  
 423 greatest at the sites with the greatest LAI, such as IT-Cpz and PhaDin.



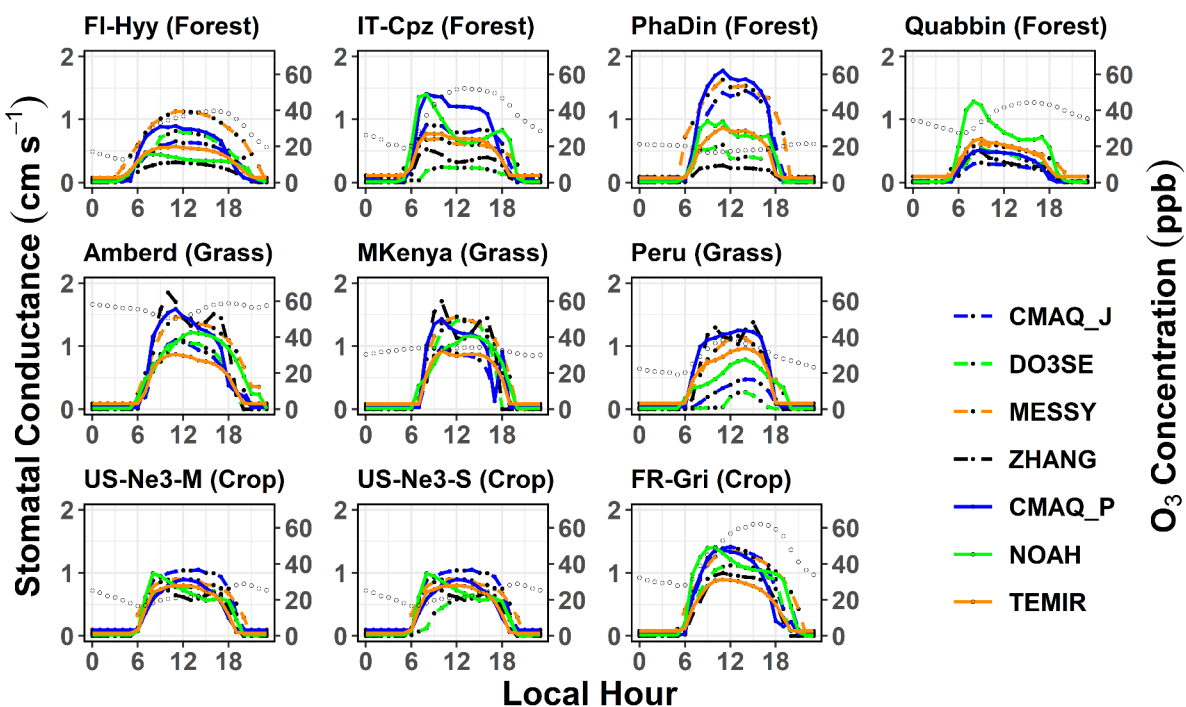
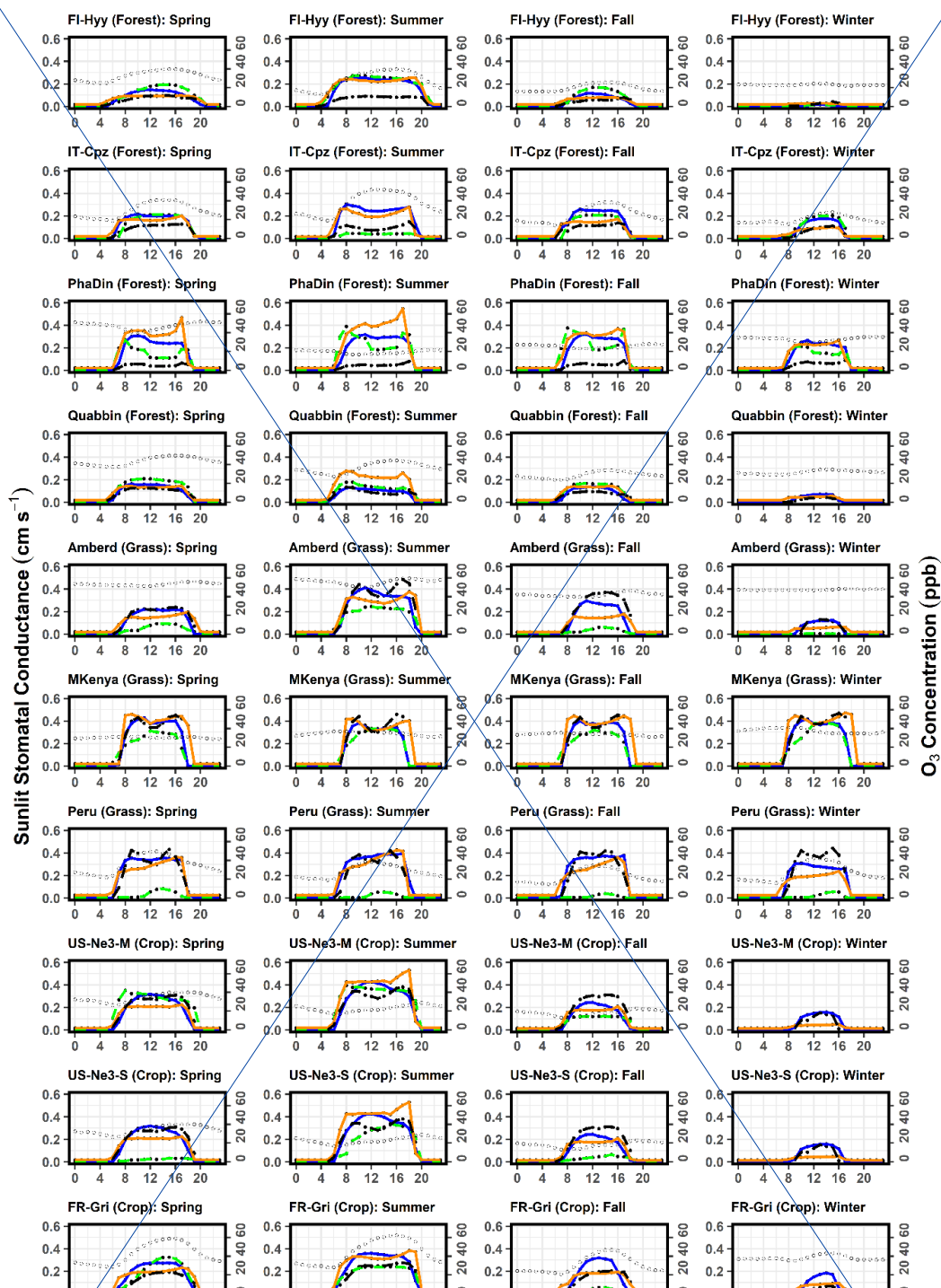
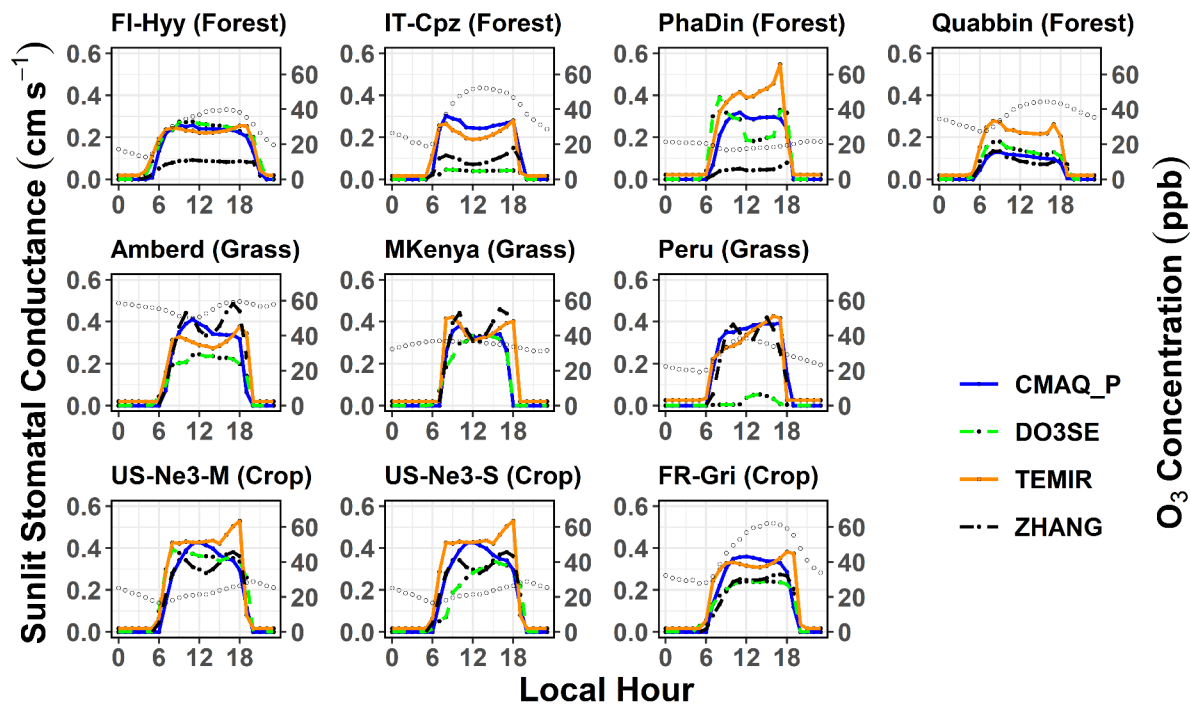


Fig. 3 Multi-year Mean diurnal cycle of growing season total stomatal conductance ( $G_{st}$ ) from models at 9 different across various sites. Four topmost panels are during the forest sites, three panels in the middle are grass sites, and three lowermost panels are crop sites summer season (US-Ne3-S=soybeans, US-Ne3-M=maize). Open circles indicate diurnal  $O_3$  variations. Respective figures for the other seasons are presented in the supplement.





433

434 Fig 4 Mean diurnal cycle of leaf level sunlit stomatal conductance ( $G_{\text{sun}}$ ) from the 3 two-leaf models  
435 (CMAQ\_P, TEMIR, and ZHANG) at 9 different across various sites. Four topmost panels are during the  
436 forest sites, three panels in the middle are grass sites, and two lowermost panels are crop sites summer  
437 season (US-Ne3-S=soybeans, US-Ne3-M=maize). Open circles indicate diurnal  $\text{O}_3$  variations. Respective  
438 figures for the other seasons are presented in the supplement.

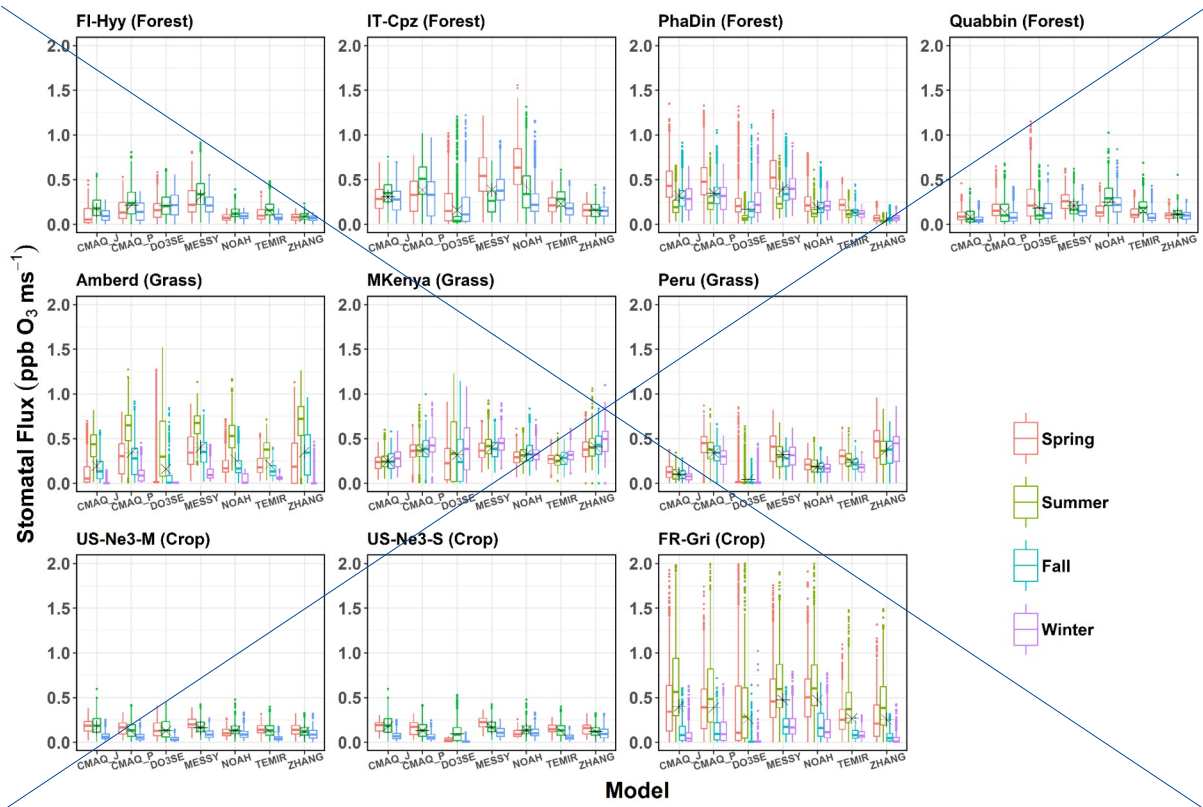
439

440 The difference between total and sunlit stomatal flux is examined, and trends of stomatal sunlit flux are  
441 characterized by different land cover types and climate conditions. Figures 5 and 6 show the ( $\text{SRAD} > 50 \text{ Wm}^{-2}$ )  
442 stomatal  $\text{O}_3$  flux ( $F_{\text{st}}$ ) and stomatal, sunlit  $\text{O}_3$  flux ( $F_{\text{st,sun}}$ ) for different models per season at 9 sites representing  
443 forest (top), grass (middle), crops (bottom). Thereby, we consider whether  $G_{\text{st}}$  and  $\text{O}_3$  concentration co-variate at  
444 diurnal and seasonal timescales. Across all land cover types, a large range of  $F_{\text{st}}$  ( $0.05\text{-}2 \text{ ppb m s}^{-1}$ , Fig. 5) is

estimated, usually highest in spring and summer and lowest in winter. The largest median of  $F_{st}$  is found at Amberd (0.75 ppb m s<sup>-1</sup>; ZHANG, summer), followed by IT-Cpz (0.60 ppb m s<sup>-1</sup>; NOAH, spring), and FR-Gri (0.60 ppb m s<sup>-1</sup>; MESSy and NOAH, summer) owing to both higher  $G_{st}$  and  $O_3$  concentrations at the respective sites (Fig. 3). Consequently, no general trend can be identified among the sites, i.e. flux estimates can differ within one land cover type. Namely, the two crop sites show very different  $F_{st}$  estimates (Fig. 5) since they have the most different  $O_3$  levels across one land cover type. While the FR-Gri site is exposed to an annual mean  $O_3$  of 45 ppb (Table S1) as the lowest  $O_3$  level of 25 ppb among all sites. The same applies for the diurnal variation of  $O_3$  causing either a high (FR-Gri) or a low range (US-Ne3) of flux estimates among all models (in summer and spring). The difference is less apparent in the  $F_{st,sun}$  estimates (Fig. 6) which point to the sensitivity of the two leaves to  $O_3$  concentration. Similarly, as seen for the stomatal conductance, three of four models show a very good agreement of  $F_{st}$  and  $F_{st,sun}$  among each other. In terms of seasonality, models agree also generally well among the grassland sites. Among those (and all land cover types), the maximum annual median  $F_{st,sun}$  was estimated for Amberd attributed to the high daytime (7 am - 7 pm) annual  $O_3$  concentrations (49.3 ppb, Table S1). The most different  $F_{st,sun}$  (and  $F_{st}$ ) values are found between the ZHANG (highest) and Web-DO<sub>3</sub>SE model (lowest) due to the difference in  $G_{sun}$  (Fig. 4). Web-DO<sub>3</sub>SE disagrees the most with the other models and predicts very small fluxes at the Peru site following the small  $G_{st}$  and  $G_{sun}$  values (Fig. 3 and 4).

Among forest sites, spring  $F_{st,sun}$  values are comparably high as summer fluxes following the seasonal variation of  $G_{sun}$  (Fig. 6, outside the tropics). The highest spring estimates at PhaDin and Quabbin (forests) are linked to the site-specific yearly  $O_3$  maximum in this season (Fig. 3). The flux seasonal maximum is more pronounced in all four models (ZHANG, CMAQ\_P, TEMIR) when the  $O_3$  concentration variation during the year is larger at the respective site. The highest  $F_{st,sun}$  (0.1 ppb m s<sup>-1</sup>) is estimated by TEMIR at PhaDin (spring) reflecting the high  $G_{sun}$  estimate. In contrast, when considering the total  $F_{st}$ , CMAQ\_P shows the highest estimate (Fig. 5) which indicates that TEMIR uses a higher sunlit fraction than CMAQ\_P as it has been shown for stomatal conductance (Fig. 3 and 4). The difference is most apparent at high LAI sites (PhaDin, IT-Cpz, FR-Gri). The lowest estimates of  $F_{st,sun}$  (and a very small spread) at the forest sites are shown by the ZHANG model as it has been explained for  $G_{st}$  and  $G_{sun}$ . Overall, CMAQ\_P has the lowest spread among the models which was also found in the multi-model comparison study by Clifton et al. (2023).





473



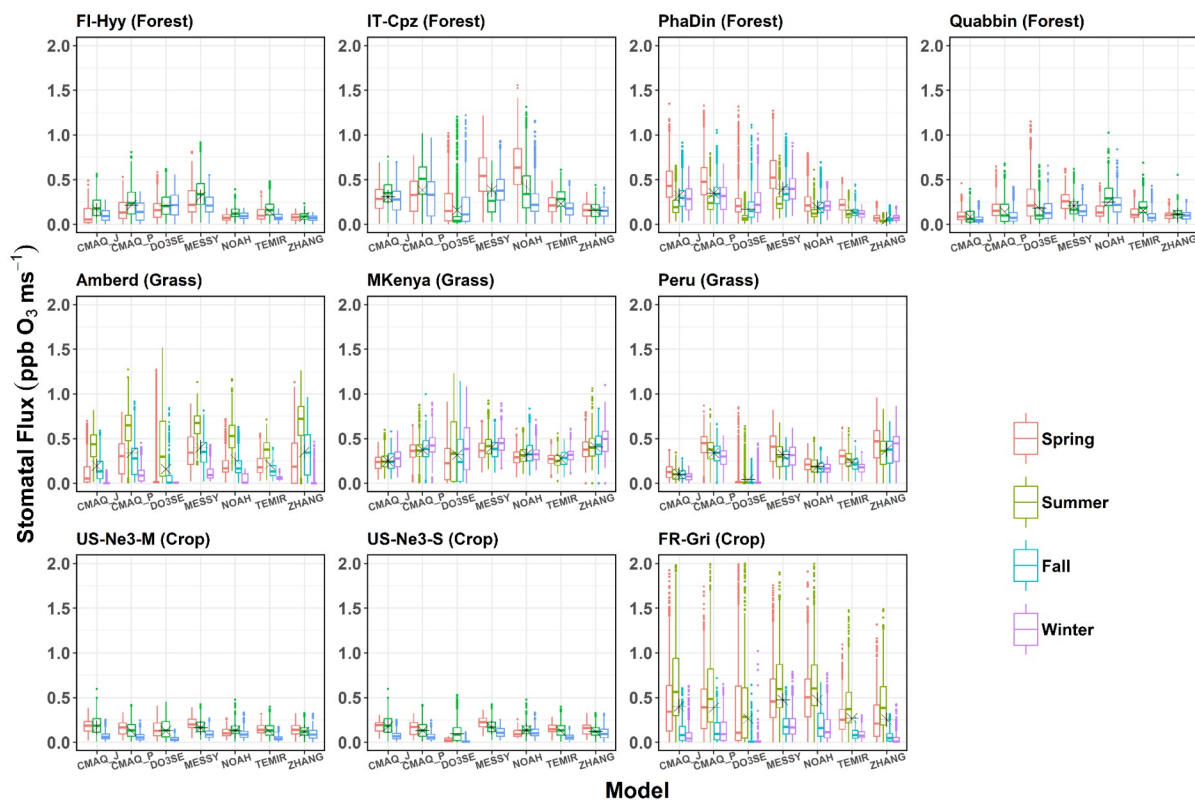
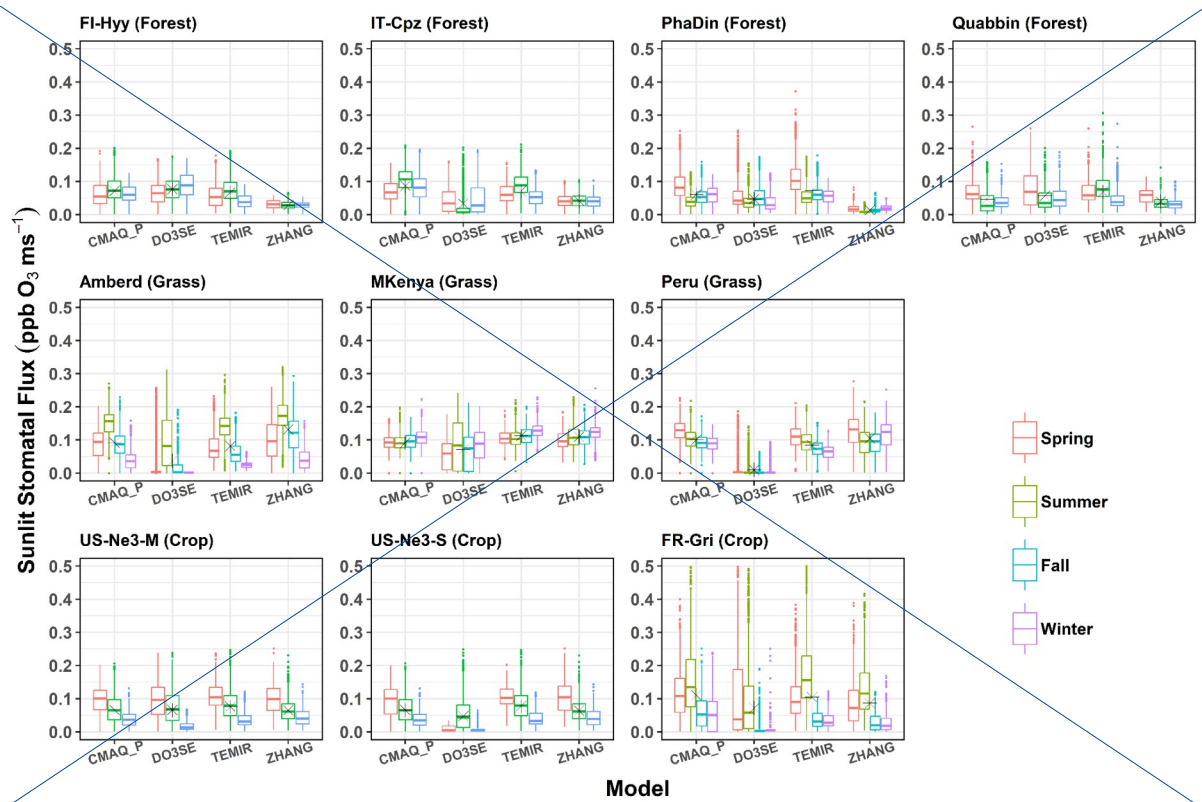


Fig 5: Boxplots of seasonal mean canopy-level total stomatal  $O_3$  flux ( $ppb\ ms^{-1}$ ) for different models at the different across various sites (data represent  $SRAD > 50\ W\ m^{-2}$  and the growing period).



477

**Fig 6: Boxplots of seasonal mean leaf-level sunlit stomatal  $O_3$  flux ( $ppb\ ms^{-1}$ ) for different models at the different 9 across various sites (data represent  $SRAD > 50\ W\ m^{-2}$  and the growing period).**

### 3.2 Vegetation impact and variation with key input data

This section presents the  $POD_y$  calculated from the  $O_3$  deposition by different models at 9 different stations to identify trends and patterns of  $POD_y$  among land cover types and climates (Fig. 7, corresponding data in Table S9). The critical threshold for ozone damage  $y$  differs for the three land cover types. For forests and grass the  $y$  value is  $1\ nmol\ O_3\ m^{-2}\ s^{-1}$  ( $POD_1$ ) while  $O_3$  damage to crops is assumed to occur only when the  $y$  threshold exceeds  $6\ nmol\ O_3\ m^{-2}\ s^{-1}$  ( $POD_6$ ). By driving the models with changed input data of  $O_3$ , soil moisture, temperature, relative humidity, growing season (Fig. 8) and with changed  $V_{c_{max}}/g_{max}$  parameter (Fig. 9) we explore the sensitivity of the  $POD_y$  estimates. As shown in the previous analysis, the largest  $O_3$  uptake and thus the highest  $POD_y$  of  $28\ mmol\ O_3\ m^{-2}$  (on average among all models) is estimated over grassland sites (compared to forest and crops) (Fig. 7).  $POD_1$  increases linearly with time for evergreen grasslands whereas Mt. Kenya shows the fastest accumulation (due to the highest  $F_{st}$  in spring and summer). Three of the four models lie in a range of  $5\ mmol\ O_3\ m^{-2}$  whereas Web- $DO_3SE$  predicts a maximum  $POD_y$  of  $10\ mmol\ O_3\ m^{-2}$  at all grassland sites. Only at the Peru site, these low values can be reasoned by the significantly lower  $G_{sun}$  and  $F_{st,sun}$  (compared to other models).

For forests, our modelled ensemble  $POD_1$  median and maximum values (ranging between  $8$  and  $25\ mmol\ O_3\ m^{-2}$ ) are similar in scale to values estimated across broad geographical regions by other studies. Karlsson et al. estimated  $POD_1$  values across Europe with the highest values in mid-latitude Europe for coniferous ( $15$  to  $20\ mmol\ O_3\ m^{-2}$ ) and broadleaf ( $22$  to  $28\ mmol\ O_3\ m^{-2}$ ) forests. However, the ZHANG and the Web- $DO_3SE$  model are estimated to be significantly lower  $POD_1$  than CMAQ\_P and TEMIR at each site. These estimates average to  $16\ mmol\ O_3\ m^{-2}$ . There is no obvious pattern to which models tend to estimate higher or lower  $POD_1$  values, but these estimates are generally consistent with  $G_{sun}$  (Fig. 4) and  $F_{st,sun}$  (Fig. 6) model estimates explained by particular model constructs or parameterisations. For instance, the ZHANG model estimates low stomatal deposition and thus also  $POD_y$  over all forests. Web- $DO_3SE$  saw a low  $O_3$  uptake only due to the site conditions at IT-Cpz.

For crops, the model estimates of  $\text{POD}_6$  are a little more consistent, with modelled differences within sites only varying between  $\sim 3$  and  $11 \text{ mmol O}_3 \text{ m}^{-2}$ , however, this could in part be due to the overall lower  $\text{POD}_6$  values due to the use of the higher  $y$  threshold. Median model ensemble values range between  $\sim 7$  and  $12 \text{ mmol O}_3 \text{ m}^{-2}$  across sites.  $\text{POD}_6$  for staple crops has been estimated in other studies across Europe and globally. A European study (Schucht et al., 2020) on wheat found  $\text{POD}_6$  values up to  $\sim 4 \text{ mmol O}_3 \text{ m}^{-2}$  suggesting that our  $\text{POD}_6$  values for the FR-Gri site tend to be too high. Feng et al. (2012) estimated maximum  $\text{POD}_6$  values of up to  $8 \text{ mmol O}_3 \text{ m}^{-2}$  for winter wheat in China though these higher values are likely driven by higher ozone concentrations. Similarly, Wang et al. (2022) also found  $\text{POD}_6$  values for maize of up to  $8 \text{ mmol O}_3 \text{ m}^{-2}$ . Our models give the largest range in  $\text{POD}_6$  estimates for soybeans at the US-Ne3 site ( $0$  to  $11 \text{ mmol O}_3 \text{ m}^{-2}$ ). A key determinant of the range in  $\text{POD}_y$  simulated by our models, and also with estimates provided in the literature, is the value chosen for  $g_{\text{max}}$  (or  $V_{\text{Cmax}}$  depending on the model construct). For example, the multiplicative  $g_{\text{sto}}$  models used to derive flux-response relationships (see Table 5) use  $g_{\text{max}}$  values of  $450$ ,  $126$  and  $301 \text{ mmol O}_3 \text{ m}^{-2} \text{ s}^{-1}$  for wheat, maize and soybeans (UNECE LRTAP, 2017; Peng et al., 2019 and Zhang et al., 2017). By contrast, our modelling uses a variety of  $g_{\text{max}}$  values, for example, the Web-DO<sub>3</sub>SE model uses  $450$ ,  $305$  and  $300 \text{ mmol O}_3 \text{ m}^{-2} \text{ s}^{-1}$  for wheat, maize and soybeans. A further consideration in parameter selection are local conditions, a study by Stella et al., (2013) found a  $g_{\text{max}}$  value of  $296 \text{ mmol O}_3 \text{ m}^{-2} \text{ s}^{-1}$  was most appropriate to describe wheat  $g_{\text{sto}}$  at the FR-Gri site. This variation highlights the importance of selecting appropriate model parameterisation for conditions, as well as consistency of parameterisation with models used to develop flux response relationships.

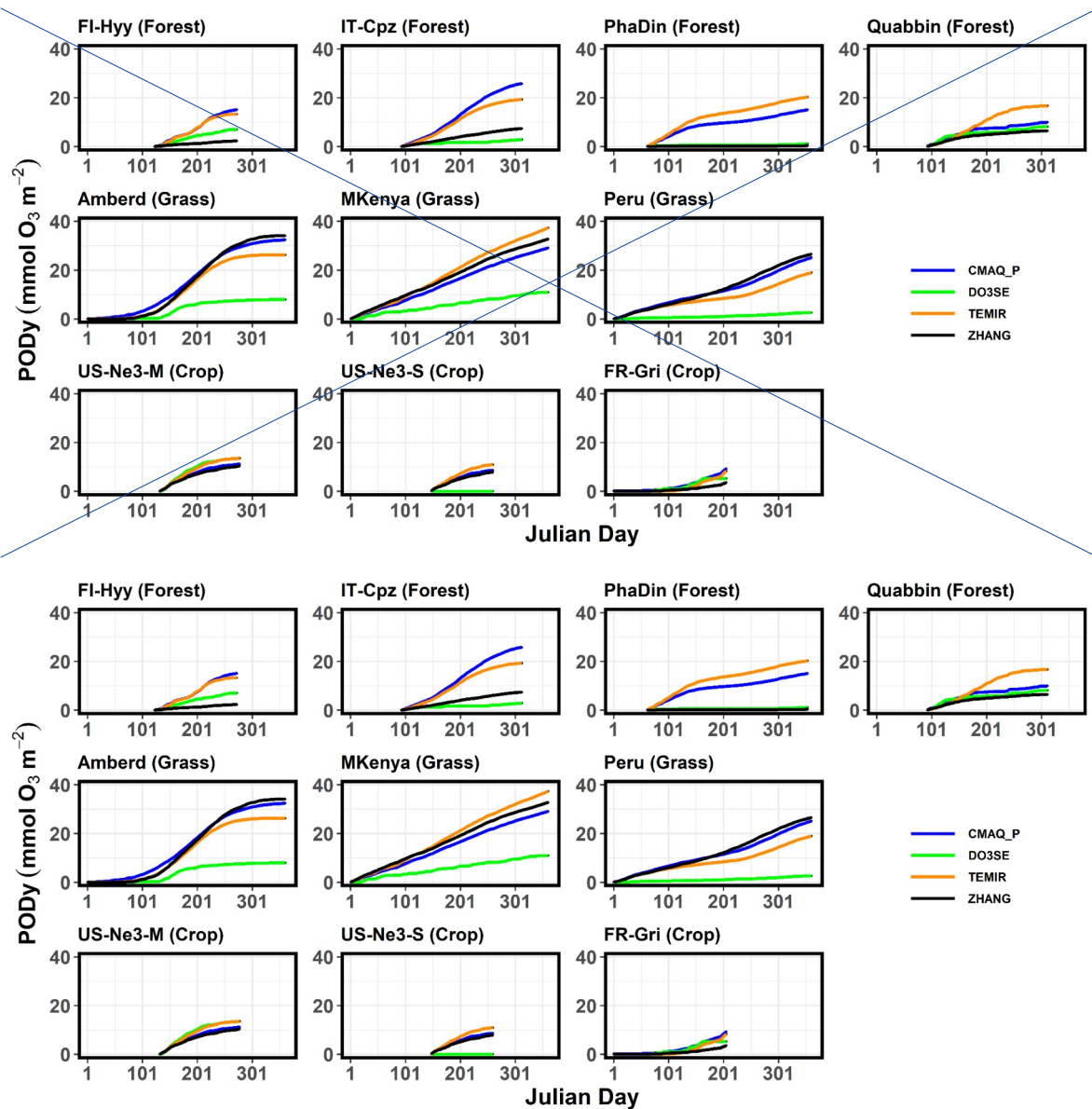
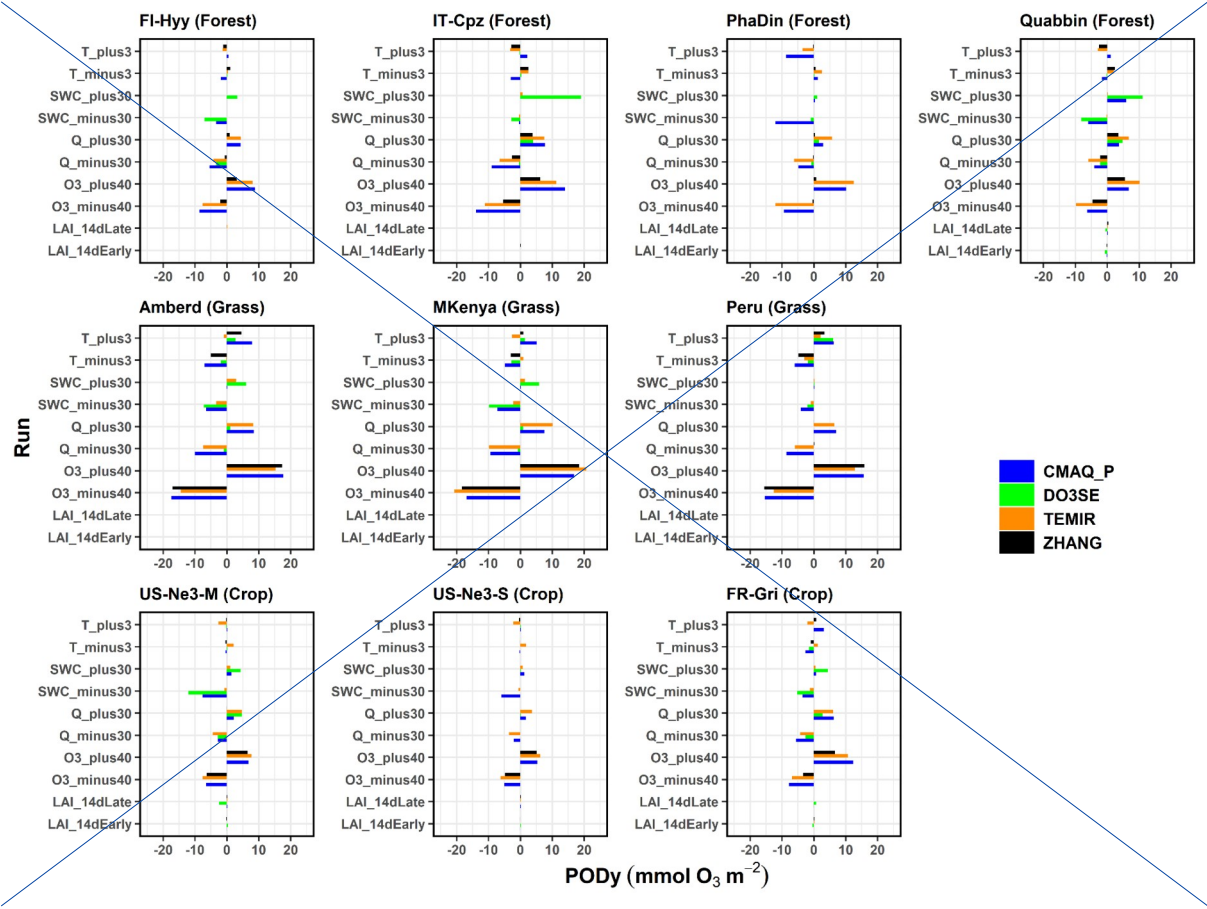


Fig 7: Evolution of  $POD_y$  (mmol  $O_3$  m $^{-2}$ ) through the growing seasons at various sites.

523 From the sensitivity analysis, we found that all models show sensitivity of  $POD_y$  to changes in  $O_3$ , specific  
 524 humidity, and temperature with varying degrees over different land cover types possibly due to different

prescribed values such as the temperature threshold (Fig. 8, corresponding absolute values in Table S10). Especially, the  $POD_y$  at all sites is most significantly changed when modifying the  $O_3$  concentration by  $\pm 40\%$  (Table S11). Crop is the most sensitive land cover to  $O_3$  changes across the different models ( $8.5 \text{ mmol } O_3 \text{ m}^{-2}$ ; 76 %  $POD_y$  change with respect to the base run), followed by forest ( $10.0 \text{ mmol } O_3 \text{ m}^{-2}$ ; 59.3%) and grass ( $14.9 \text{ mmol } O_3 \text{ m}^{-2}$ ; 56.1%) which is due to the plant physiognomy (Grulke and Heald et al. ,2020). In a relative sense, the average response change in  $POD_y$  to a 40 % change in  $O_3$  concentrations is the greatest in ZHANG ( $+9.2 \text{ mmol/m}^2 \text{ } O_3 \text{ m}^{-2}$ , corresponding to a 68.1 %  $POD_y$  change with respect to the base run), followed by CMAQ\_P and TEMIR (12 and  $11.9 \text{ mmol } O_3 \text{ m}^{-2}$  ;64.8 % and 63.5 %), and then by Web-DO<sub>3</sub>SE ( $11.4 \text{ mmol } O_3 \text{ m}^{-2}$ ; 53.0 %). Also, the  $POD_y$  estimate seems to be sensitive to humidity (Q) changes ( $\pm 30\%$ ) among all models. At forest, the  $POD_y$  estimates appear to be the most sensitive ( $4.6 \text{ mmol/m}^2 \text{ } O_3 \text{ m}^{-2}$ ; 27.3%), followed by crops ( $2.9 \text{ mmol } O_3 \text{ m}^{-2}$ ; 25.9%) and grass ( $4.6 \text{ mmol } O_3 \text{ m}^{-2}$ ; 17.3 %). The response is the greatest in TEMIR and CMAQ (between  $5.7$  and  $6.7 \text{ mmol } O_3 \text{ m}^{-2}$ ; 30.7-35.8 %), while it is much smaller for ZHANG (usually close to zero on average). The most non-linear response was shown by Web-DO<sub>3</sub>SE at IT-Cpz which estimated a 5 times higher  $POD_y$  response to increasing humidity than to a humidity decrease pointing towards the strong dryness at this site limiting. If temperature is changed by  $\pm 3 \text{ K}$  the highest sensitivity was found at crops on average ( $2.7 \text{ mmol } O_3 \text{ m}^{-2}$ ; 24.1%), followed by grass ( $4.6 \text{ mmol } O_3 \text{ m}^{-2}$ ; 17.2 %) and forest ( $1.6 \text{ mmol } O_3 \text{ m}^{-2}$ ; 9.5%). The responses unevenly vary in sign depending on the model because the temperature change depends on the optimal temperature at the specific sites. Namely most models estimate a  $POD_y$  decrease when increasing temperature (Fig. 5). As described in Hayes et al. (2019), a temperature increase is seen in southern countries where temperature could limit stomatal uptake since temperature is already close to the optimum in normal conditions. From our sensitivity analysis, temperature impacts on  $POD_y$  are noticeable only for a few sites (e.g., Ambered, Mt. Kenya, and Peru) and models's response to  $POD_y$  change were different due to different thresholds used for the temperature stress factors to stomatal conductance. The greatest changes in magnitude are predicted by Web-DO<sub>3</sub>SE ( $5.1 \text{ mmol } O_3 \text{ m}^{-2}$ ; 23.7%), followed by CMAQ\_P ( $3.1 \text{ mmol } O_3 \text{ m}^{-2}$ ; 16.7%), ZHANG ( $1.9 \text{ mmol } O_3 \text{ m}^{-2}$ ; 14.1 %) and TEMIR ( $1.7 \text{ mmol } O_3 \text{ m}^{-2}$ ; 9.6 %). In contrast, not all models are sensitive to changes of soil water content (SWC). The greatest response is seen in CMAQ\_P ( $-6.3$  and  $+1.4 \text{ mmol } O_3 \text{ m}^{-2}$ ; -34.0% and +7.6%), followed by Web-DO<sub>3</sub>SE ( $-2.2$  and  $-2.2 \text{ mmol } O_3 \text{ m}^{-2}$ ; -10.2% and -10.2%), and TEMIR ( $-1.1$  and  $+0.8 \text{ mmol } O_3 \text{ m}^{-2}$ ; -5.9% and +4.3%), while ZHANG shows no difference in this regard because it is not sensitive to soil moisture. The changes are largest at crops ( $1.5 \text{ mmol } O_3 \text{ m}^{-2}$ ; 13.4%), while grass and forest show similar responses ( $2.8$  and  $1.7 \text{ mmol } O_3 \text{ m}^{-2}$ ; 10.5 and 10.1 %, respectively). That is in line with De Marco et al. (2020) who show that  $POD_y$  responses to soil water changes increase with higher Y threshold (here crops). The models

do not appear to be sensitive to LAI 14d shifts, with the only exception of Web-DO<sub>3</sub>SE, which simulates a lower POD<sub>y</sub> for both early and late LAI shifts (-2.6 mmol O<sub>3</sub> m<sup>-2</sup> on average, across all land covers). LAI is used as a proxy for growing seasons in most models ~~whereas Web-DO<sub>3</sub>SE considers growing seasons~~ directly.





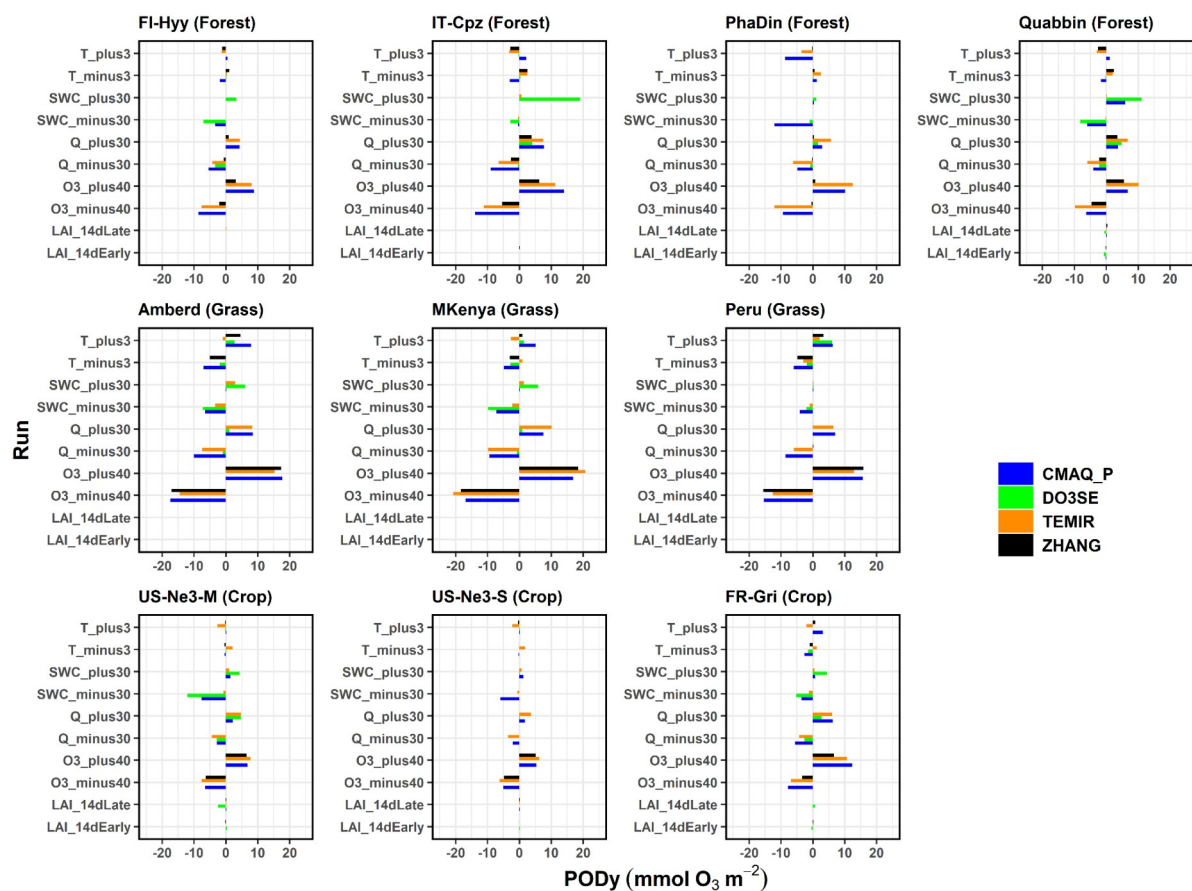
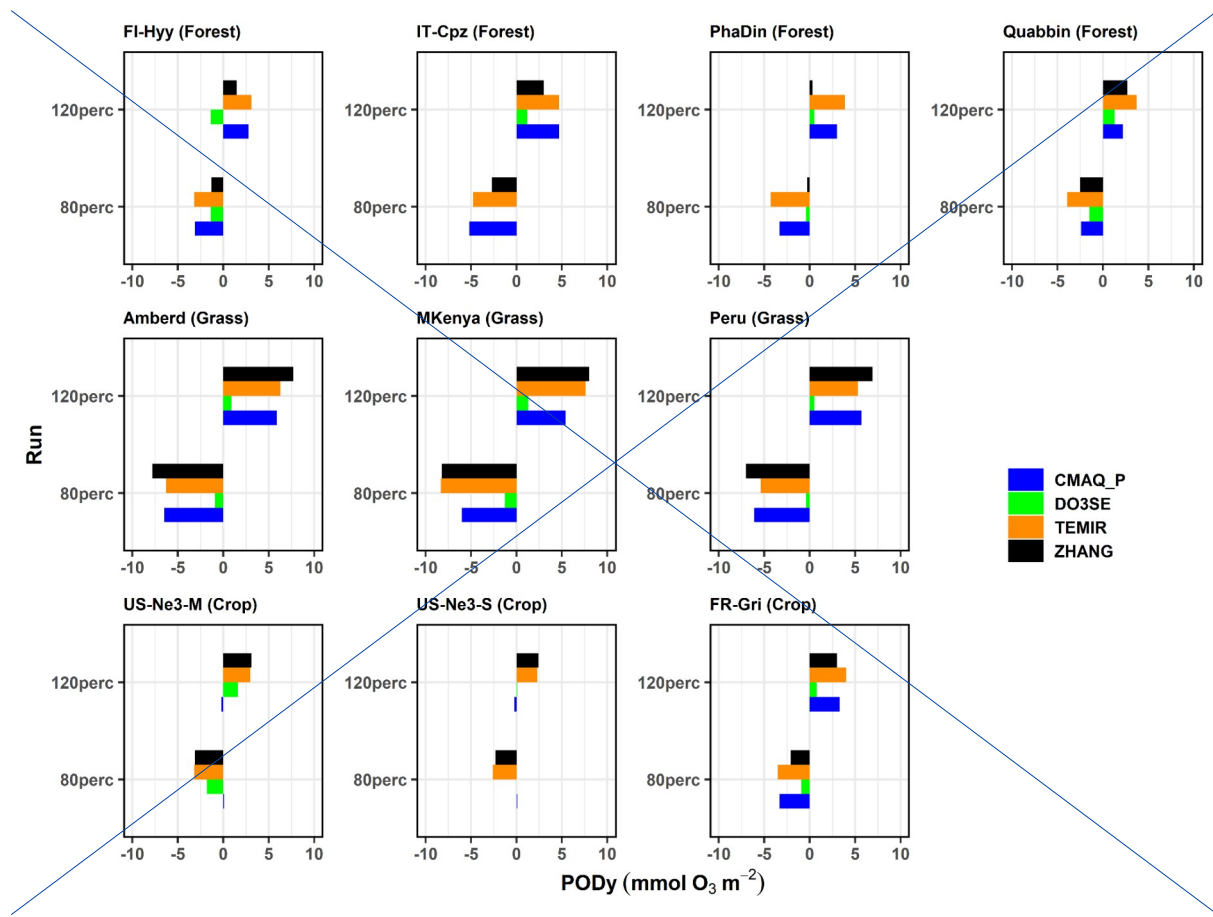


**Fig 8: Meteorology sensitivity assessment: Absolute change of  $POD_y$  values with respect to Base run  $POD_y$  due to 10 or 20 % variation of the temperature (T), soil water content (SWC), absolute humidity (Q),  $O_3$  and LAI/growing season.**

A 20% change of  $g_{max}/Vc_{max}$  leads to corresponding changes in  $POD_y$  values. An increase or decrease of the parameter leads to very similar changes (in +/-) (Fig. 9, corresponding data in Table S12 – S14). The response appears to be generally uniform across sites. On average, the results show  $+28.9 \pm 22.4$  %  $POD_y$  change for the 20 % increase of  $g_{max}/Vc_{max}$ , and  $-27.4 \pm 13.1$  % for the 20 % decrease with the largest absolute changes at grassland (up to  $8 \text{ mmol } O_3 \text{ m}^{-2}$ , ZHANG). At forests and crops, changes up to 5 and  $3 \text{ mmol } O_3 \text{ m}^{-2}$  occur,



respectively. Among all sites, noticeably higher (the highest) relative changes were estimated at FR-Gri which thus constituted the only relevant source of variability. This change is significantly different to the change at US-Ne3 (20-30 %) which reflects the contrasting low O<sub>3</sub> level at US-Ne3 compared to the highly polluted FR-Gri site. Also, the ZHANG model predicts the highest changes at crops while CMAQ\_P seems insensitive. The ZHANG (and TEMIR) model appears to be the most sensitive model to the changes at most sites due to the strong dependency on the  $g_{\max}/V_{c\max}$  parameter (see analysis above). The only climate trend of the response is seen by the ZHANG model which shows an average 65 % increase/decrease in wet forests (PhaDin, FI-Hyy) and only a 40 % change in dry places. Sites with very low estimates (PhaDin in ZHANG, Peru in Web-DO<sub>3</sub>SE) were excluded from this sensitivity study.



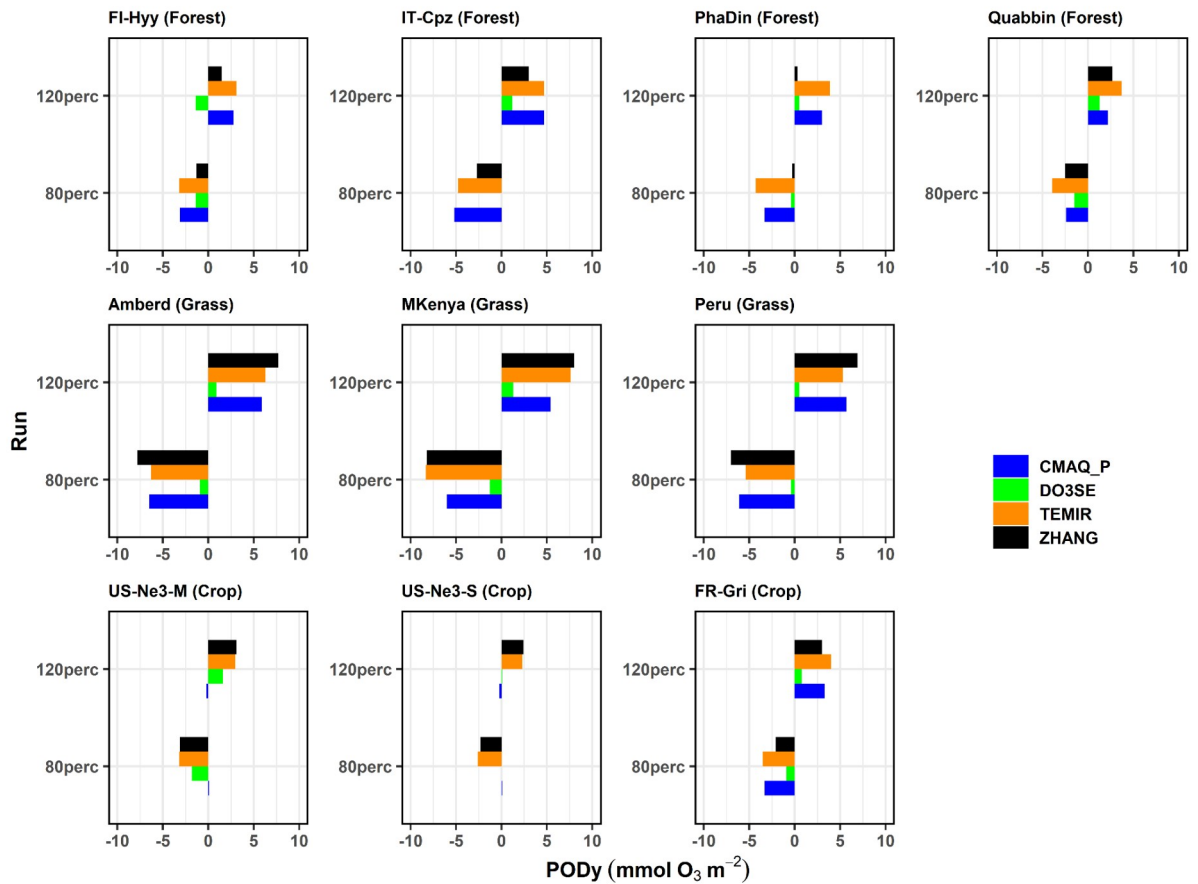


**Fig 9: Land cover parameterisation sensitivity assessment: Absolute change of  $POD_y$  values with respect to the base run  $POD_y$  values due to 20 % variation of  $G_{max}$  or  $V_{Cmax}$ .**

To indicate the likely damage, and range of damage that our modelled values of  $POD_y$  predict, we have used  $POD_y$  flux-response relationships available in the literature that most closely represent the vegetation type and climatic location of each study site (Table 5). To estimate  $O_3$  damage to forests we use recently derived flux-response relationships that relate  $POD_1$  values to gross annual increment (Karlsson et al., sub) and hence indicate the annual change in growth rate caused by  $O_3$ . The mean model ensemble estimates a percentage reduction in gross annual increment of around 5% for FI-Hyy and Pha Din, 6% for IT-Cpz and 14% for Quabbin. However,

593 the range in estimates across models is not insignificant and most extreme at the Quabbin site with a minimum  
594 of 11% and a maximum of 21% around the mean 13% value; this is due to broadleaf deciduous species being  
595 more sensitive to O<sub>3</sub> dose than needleleaf species and hence more sensitive to a range of POD<sub>y</sub> model  
596 simulations (Bueker et al., 2015). It should also be emphasised that the Pha Din site uses a European-derived  
597 flux-response relationship for an Asian forest site.

						PODy	-		% Respon se			
Site	Species	y	Flux- response relationship	Response metric & species	min	median	max	min	median	max	Location of PODy relationsh ip	Reference
Fl-Hyy	Scots pine	1	$y = -0.0057x + 1.0015$	Gross Annual Increment (GAI) % for Norway spruce/Scots pine	2.3	10.2	15.1	1.2	5.6	8.5	Europe	Karlsson et al., sub (to TOARII community special issue)
Quabbin	Birch/ Beech (Broadle af deciduou s)	1	$y = -0.0093x + 0.9461$	Gross Annual Increment (GAI) % for Birch/Beech	6.5	9.1	16.8	11.4	13.9	21.0	Europe	Karlsson et al., sub (to TOARII community special issue)
PhaDin	Norway spruce (Evergre en needlele af)	1	$y = -0.0057x + 1.0015$	Gross Annual Increment (GAI) % for Norway spruce/Scots pine	0.4	8.1	20.3	0.0	4.5	11.4	Europe	Karlsson et al., sub (to TOARII community special issue)
IT-Cpz	Holm oak	1	$y = -0.0047x + 1.001$	Gross Annual Increment (GAI) % for Aleppo pine/Holm Oak	2.8	13.3	25.8	1.2	6.2	12.0	Europe	Karlsson et al., sub (to TOARII community special issue)
FR-Gri	winter wheat	6	$y = -0.0385x + 1.003$	% grain yield loss for wheat	3.6	6.8	9.3	13.6	25.9	35.5	Europe	UNECE LRTAP Mapping Manual (2017)
US- Ne3 (Maize )	Maize	6	$y=0.0426x+1$	% grain yield loss for wheat	10.5	12.4	13.6					Peng, J., Shang, B., Xu, Y., Feng, Z., Pleijel, H. and Calatayud, V., 2019. Ozone exposure-and flux- yield response relationships for maize. Environmen tal pollution, 252, pp.1-7.
US- Ne3 (Soybe an)	Soybean	6	$y = -0.033x + 1.01$	% relative seed yield loss per soybean plant	0.0	8.3	11.0	0.0	26.4	35.3	China	Zhang, W., Feng, Z., Wang, X., Liu, X., Hu, E. (2017) Quantification of ozone exposure- and stomatal uptake-yield response relationships for soybean in Northeast China. Sci of the Total

												Env., 599-600 (710-720)	
Amber d	Grasslan d	1	$y = -0.0062x + 0.947$	% total biomass loss for temperate perennial grassland	7.9	29.4	34.1	10.2	23.5	26.4	Europe	UNECE Mapping (2017)	LRTAP Manual
MKenya	Grasslan d	1	$y = -0.0062x + 0.947$	% total biomass loss for temperate perennial grassland	10.9	31.0	37.4	12.1	24.5	28.5	Europe	UNECE Mapping (2017)	LRTAP Manual
Peru	Grasslan d	1	$y = -0.0062x + 0.947$	% total biomass loss for temperate perennial grassland	2.6	22.1	26.6	6.9	19.0	21.8	Europe	UNECE Mapping (2017)	LRTAP Manual

**Table 5. Estimates of O<sub>3</sub> damage (for specific response metrics) derived from using the ensemble mean modelledmodeled PODy values (and minimum and maximum values) with appropriate flux-response relationships based on land cover type. The climatic location within which the flux-response relationships are derived are stated to show the relevance of their use in estimating damage. Shaded cells denote flux-response relationships that are derived outside of the broad climate region to which they are applied in this study and hence whose damage estimates should be treated with caution.**

For crops, flux response relationships are available for wheat, maize and soybeans (UNECE LRTAP, 2017, Peng et al., 2019 and Zhang et al., 2017). These relationships are derived from Europe (wheat) and China (maize and soybean). For wheat, we see a large range in percentage yield loss with a mean model ensemble of 26 % but a maximum yield loss of 35 %. This is driven by high POD<sub>6</sub> values derived from CMAQ\_P and TEMIR. For maize at US-Ne3 the results are very consistent with relative grain yield loss estimates ranging from 1.4 to 1.6 %. For soybeans at US-Ne3, the results are less consistent than maize with a minimum and maximum of 0 and 35 % yield around a mean of 26 %. It is important to note that a Chinese-derived flux-response relationship is used to estimate O<sub>3</sub> damage on both US-grown crops.

616 Finally, for grasslands, we estimate total biomass losses of 19, 24 and 23% from the ensemble model mean for Peru, Mt  
617 Kenya and Amberd respectively. The range in model values is relatively small for Amberd and Mt Kenya. A low minimum  
618 value of 6 % total biomass loss is estimated for Peru due to the Web-DO<sub>3</sub>SE model having a very low POD<sub>y</sub> at this location  
619 due to a likely oversensitive limitation to O<sub>3</sub> uptake caused by low temperatures.

620

#### 621 4. Discussion and Conclusion

622 Here we have compared six deposition schemes commonly used in atmospheric chemistry transport models. We have  
623 focussed on the stomatal component of deposition since this is acknowledged to have a substantial influence on damage to  
624 vegetation, and ultimately the ability of these six models to estimate the POD<sub>y</sub> metric designed to indicate the level of O<sub>3</sub>  
625 damage to forest, crops and grasslands. The models estimate POD<sub>y</sub> values of 28, 15 and 9 mmol O<sub>3</sub> m<sup>-2</sup> for grassland, forests  
626 and crops, respectively. The multi-model mean estimates are generally in the expected range which suggests that the  
627 stomatal flux output of these models could be used for O<sub>3</sub> impact assessments. We also explored the differences in POD<sub>y</sub> by  
628 geographical location. When comparing one vegetation type, we find multiple drivers including O<sub>3</sub> concentration. The  
629 different model types are not the driving force, instead, the models can predict similar results.

630 There are three key reasons for differences in dry deposition model estimates i. model construct and the inclusion/exclusion  
631 of important factors that determine G<sub>st</sub> and G<sub>sun</sub>; ii. model parameterisation which may characterise the land cover types and  
632 iii. differing model sensitivity to climate variables (seasonal, location effects) in estimates of stomatal deposition. The model  
633 comparison of stomatal conductance and stomatal dry deposition for ozone helps us to understand the differences between  
634 models. We found that models simulate generally reasonable stomatal deposition of 0.5 -0.8 cm s<sup>-1</sup> in summer whereas the  
635 different model types often agree very well with each other. The stomatal conductance estimates among the models agree  
636 with correlation coefficients of 0.75, 0.80 and 0.85 for forests, crops and grasslands. Thereby, the 9 sites selected for this  
637 study also reflect different climate conditions; however the selection of sites that provide such broad representations also  
638 means that the analysis and the results cannot be generalized. The global coverage, diverse land types and varying  
639 meteorological conditions of the 9 sites resulted in widespread model responses to soil moisture (Fig. 8), while appearing to  
640 be insensitive to changes of LAI (Fig. 9). The former underscored the idiosyncratic features and hence potential limitations  
641 of individual models, whereas the latter gave us confidence in model capabilities despite the different constructs and  
642 parameterizations of the models. The model differences, identified during this analysis, can be explained by the model's  
643 dependence on the meteorological conditions at sites. Indeed, both model structure (e.g. Raghav, Kumar and Liu 2023) and  
644 parameters (Fares et al., 2013) can affect the accuracy of stomatal conductance models. However, studies have shown that  
645 when properly calibrated against field observations, structurally different stomatal models can produce similar stomatal

646 conductance (Fares et al., 2013, Mäkelä et al., 2019). Calibrating the key parameters of stomatal conductance models (e.g.  
647  $g_{\max}/V_{c_{\max}}$ ) is a crucial next step to improve the accuracy of stomatal conductance and  $POD_y$  estimates, as our sensitivity tests  
648 show direct, and possible non-linear relationship between  $POD_y$  and  $g_{\max}/V_{c_{\max}}$  (e.g. at FR-Gri). This is possible with the  
649 recent availability of standardised global eddy flux (FLUXNET, Pastorello et al., 2020) and sap flow (SAPFLUXNET,  
650 Poyatos et al., 2020) data.

651 To estimate  $POD_y$  for a representative leaf of the upper canopy, the sunlit leaf must be distinguished from the total leaf.  
652 Since the effects-based community recognised that sunlit leaves contribute most to carbon assimilation throughout the  
653 growing season or  $O_3$ -sensitive period (e.g. in wheat, this is considered to be the time from anthesis to maturity) and hence it  
654 will better represent damaging  $O_3$  uptake. All flux response relationships for  $POD_y$  are developed for such a representative  
655 leaf. This is an important distinction since previous model comparison studies (e.g. Clifton et al., 2023) have tended to focus  
656 on whole canopy dynamics. These are important to estimate accurately, but to estimate  $POD_y$  requires additional canopy  
657 level processes, which need i.  $O_3$  concentration at the top of the canopy, ii. wind speed at the top of the canopy and iii.  $G_{\text{sun}}$  of  
658 a representative leaf at the top of the canopy. Studies (Emberson 2020 and references therein) have established thresholds for  
659 different land cover types which are used to provide  $y$  values for the selected sites with specific land cover types in this  
660 study. Some studies suggest that the  $y$  threshold for land cover types may vary by global region (e.g. a number of studies  
661 suggest higher  $y$  values of up to  $12 \text{ nmol } O_3 \text{ m}^{-2} \text{ s}^{-1}$  is more appropriate for crops and forest tree species in Asia). In this study,  
662 which focuses on comparing across models, we maintain consistency and use common  $y$  threshold values for each land  
663 cover type. However, this is an aspect that would benefit from further study in the future since estimating  $POD_y$  values with  
664 higher thresholds is more challenging for all types of model given the less frequent occurrences of such high  $O_3$  doses.

665 Our models estimate 30-50 % of stomatal  $O_3$  deposition at sunlit leaves. Thereby, the model estimates of the total stomatal  
666 flux are more widespread (during one season) than the estimates of the sunlit only which suggests an important role of the  
667 model's partitioning in two big leaves. When calculating  $POD_y$  model means estimates generally agree with the literature but  
668 most discrepancies between model estimates of  $POD_y$  ultimately come down to the differences in simulations of stomatal  
669 conductance. The sensitivity analysis of  $POD_y$  yields ozone as the most important input variable, to whose changes all  
670 models respond similarly. Considering all models and sites together,  $POD_y$  were affected most by the  $O_3$  concentration (+/-  
671 60-80 % site-dependent, i.e., higher  $O_3$  ~~one~~concentration leads to higher  $POD_y$ ), followed by humidity (30-50 % site-  
672 dependent impact). Soil moisture impacts were also significant for the CMAQ\_P and Web- $DO_3$ SE model (up to +/-68 % and  
673 22 % change). The sensitivity to temperature changes varies strongly among the model and its parametrization. As the plant  
674 canopy acts as a persistent sink of  $O_3$ , there is a significant vertical gradient of  $O_3$  within the atmospheric surface layer. For  
675 example, Travis et al. (2019) show that the midday  $O_3$  concentration at 65 m above ground (mid-point of a first vertical layer  
676 of GEOS-Chem v9-02) is 3 ppb higher than the  $O_3$  concentration at 10 m above ground (inferred by Monin-Obukhov  
677 Similarity Theory, MOST) over the Southeastern United States. A mismatch between  $O_3$  measurement height and canopy

678 height can lead to inaccurate  $\text{POD}_y$  calculation (Gerosa et al, 2017). [As An O3 bias of 2 ppb as estimated by e.g. Tarasick et](#)  
679 [al. \(2018\) would lead to a change of 6-7 % in  \$\text{POD}\_1\$  \(Gerosa et al., 2017\). Similarly,](#) we show that the errors in  $\text{O}_3$   
680 concentrations propagate non-linearly to  $\text{POD}_y$  (i.e. 40% changes in  $\text{O}_3$  leads to 53 - 68 % changes in  $\text{POD}_y$ ), such a  
681 mismatch should be carefully avoided by applying atmospheric surface layer theories (e.g. MOST) to estimate the vertical  
682 profile of  $\text{O}_3$ , and therefore the canopy-top  $\text{O}_3$  concentration, if direct measurement or model output of  $\text{O}_3$  at canopy top is  
683 not available.

684

685 Finally, we use flux-response relationships for temperate deciduous (Beech/birch), temperate needleleaf (Norway spruce  
686 (*Picea abies*)), crops (wheat (*Triticum aestivum*), maize (*Zea mays*) and soybeans (*Glycine max*)) and grassland (*Lolium*  
687 *perenne*) to give a suggest the potential likely variation of damage estimates by land cover type and climatic region. These  
688 relationships have predominantly been developed for European and Asia forest and crop species. Therefore, they should be  
689 applied to other climate regions with caution although recent evidence suggests that tropical forest species may have similar  
690 sensitivity to  $\text{O}_3$  as European species (Cheeseman et al. 2024). Although there is rather large variability in  $\text{POD}_y$  values  
691 estimated by the model, the median values are relatively robust. Unfortunately, there is only statistical or modelled evidence  
692 of actual  $\text{O}_3$  damage, and only at a few of the sites investigated. Modelled evidence uses stomatal ozone flux models similar  
693 to those used in this study, but which have been parameterised for local site conditions (Stella et al., 2013 for FR-Gri wheat).  
694 Simulations with a terrestrial biosphere model suggested an average long-term  $\text{O}_3$  inhibition of 10.4% for the period 1992–  
695 2011 at the Harvard site (Yue et al 2016); this compares to our model ensemble estimate of 14% GAI biomass loss for  
696 Quabbin. A significant but small NEP reduction was found during Spring in the Italian Castelporziano forest site (up to -1.37  
697 %) but not at the FI-Hyy or FR-Gri sites (Savi et al., 2020). Our modelling estimated substantially lower  $\text{POD}_y$  values and  
698 associated damage at Hyy and IT-Cpz than Quabbin though we would expect to see a more substantial  $\text{O}_3$  effect than that  
699 demonstrated by the NEP statistical modelling (i.e. 5 and 6% GAI biomass loss at FI-Hyy and IT-Cpz respectively). Similar  
700 simulations with a different terrestrial biosphere model found only moderate  $\text{O}_3$  damage effects (GPP reductions of 4–6 %;  
701 Yue & Unger, 2014). This result is driven by low ambient ozone concentrations but also by the choice of a C4  
702 photosynthetic mechanism to estimate stomatal conductance which gives relatively high-water use efficiency). These  
703 simulations also suggested that the US-Ne3 experienced a higher ozone effect on GPP than Harvard which is consistent with  
704 our modeling for soybeans (but not maize, generally considered an  $\text{O}_3$  tolerant crop species; Mills et al 2011). According to  
705 the  $\text{POD}_6$  estimates made using a SURFATM model, parameterised for Grignon wheat,  $\text{POD}_6$  values of  $1.094 \text{ mmol O}_3 \text{ m}^{-2}$   
706 were estimated from 1 April to 1 July 2009 which compared with our range of 3.6 to 9.3; the locally parameterised values  
707 gave estimated crop yield losses of 4.2%, compared to our median model ensemble estimates of 25% for the winter wheat.  
708 This is most likely due to the lower  $g_{\text{max}}$  value used in the local parameterisation ( $296 \text{ mmol O}_3 \text{ m}^{-2} \text{ s}^{-1}$ ). However, no

99  
100  
101



709 recording of actual damage is given at the FR-Gri site, so it is not possible to tell which of these simulated damage estimates  
710 is closer to reality.

711 The experiments performed here with varying climate and vegetation input data also find a similar sensitivity of  $POD_y$  to  $O_3$ .  
712 It is helpful to have a range of models and model constructs in deposition schemes especially where these have been  
713 developed for particular land cover types. When used in damage estimates it is important to ensure that key stressors are  
714 included which may be important for that respective geographical region (such as soil and vapour pressure deficit).  
715 Recognising that several deposition schemes would be able to reliably predict  $POD_y$  for different climates and cover types  
716 once they have been parameterised appropriately will extend the usefulness of flux-response relationships.

717 ~~All in all, we have~~Overall, this study has demonstrated, ~~through this paper,~~ the widespread applicability and consensus  
718 among various numerical stomatal flux methods ~~and. Both semi-mechanistic as well as empirical models can generally~~  
719 ~~represent observed ozone fluxes among different land cover types and climates. We~~ identified the key model constructs and  
720 parameterisations that cause differences in ~~ozone deposition and~~  $POD_y$  estimates. ~~However, none of the models clearly~~  
721 ~~shows a superior overall performance. Instead, all models can be effectively applied, each with its own strengths and~~  
722 ~~weaknesses.~~ Our ~~results and~~ findings present exciting opportunities, ~~enabling us~~ to extend ~~the application~~ applications beyond  
723 specific sites and growing seasons, ~~to conduct~~ enabling comprehensive global stomatal flux studies over ~~longer~~ longer periods.  
724 Integrating the TOAR database with the Web-DO<sub>3</sub>SE model enables automatic ~~models~~ model runs for ozone-vegetation  
725 impact assessment at a large range of sites using the TOAR database.

726  
727

## 728 Author contributions

729 T.E.: site selection, TOAR data extraction, data preparation, model support, modelling Web-DO<sub>3</sub>SE, writing, coordination.  
730 A.M.: modelling (ZHANG, MESSy, NOAH-GEM, TEMIR model), statistics, plots and analysis. ~~C.B.: debugging and test~~  
731 ~~simulations of Web-DO<sub>3</sub>SE.~~ L.E.: concept, writing. ~~\_\_\_\_\_~~ H.M.: writing, reviewing. L.Z.: concept and writing. L.R. ~~and J.P.:~~  
732 modelling with CMAQ, FLUXNET data preparation. C.B.: debugging and test simulations of Web-DO<sub>3</sub>SE. A.W.: site  
733 selection, preparation of FLUXNET and sensitivity data. G.K.: site selection, TOAR data extraction. G.G.: site analysis.  
734 M.H.: plots and reviewing. P.G.:  $POD_y$  analysis.

735

## 736 Competing interests

737 ~~Leiming Zhang is an editor with ACP.~~  
738 The authors have no competing interests.

739

102  
103  
104

740 **Acknowledgements**

741 We acknowledge the TOAR team supports the data extraction. The authors acknowledge the access to the meteorological  
742 data on the Jülich MeteoCloud provided by Jülich Supercomputing Centre (Krause et al., 2018). We thank the responsible  
743 people of the selected measurement sites for their support in obtaining site information. We greatly appreciate helpful  
744 discussions in the earlier stages of the project from the following people: Owen Cooper, Zhaozhong Feng, Laurens  
745 Ganzeveld, Meiyun Lin, Martin Schultz, Eran Tas, and Oliver Wild.

746

747 **Code availability**

748 [The Web-DO<sub>3</sub>SE source code is freely available at https://toar-data.fz-juelich.de/](https://toar-data.fz-juelich.de/) under the CC-BY 4.0 license  
749 (<https://creativecommons.org/licenses/by/4.0/>). The further model code can be obtained upon request.

750

751 **Data availability**

752 The TOAR data is freely available at <https://toar-data.fz-juelich.de/> under the CC-BY 4.0 [license](https://creativecommons.org/licenses/by/4.0/)  
753 (<https://creativecommons.org/licenses/by/4.0/>). The ERA5 data used can be downloaded from the MeteoCloud server  
754 (<https://datapub.fz-juelich.de/slcs/meteocloud/index.html>). FLUXNET 2015 dataset is publicly available at  
755 <https://fluxnet.org/data/fluxnet2015-dataset/>. Stomatal conductance estimates, and the related FLUXNET 2015 data from  
756 SynFlux version 2 can be obtained by contacting Christopher Holmes ([cdholmes@fsu.edu](mailto:cdholmes@fsu.edu)).

757

758 **References**

759 Ainsworth, E. A., Yendrek, C. R., Sitch, S., Collins, W. J., ~~&~~ Emberson, L. D.: The effects of tropospheric ozone on net  
760 primary productivity and implications for climate change. Annual review of plant biology, 63(1), 637-661, [https://doi:  
761 .org/10.1146/annurev-arplant-042110-103829](https://doi.org/10.1146/annurev-arplant-042110-103829), 2012.

762

763 Ainsworth, E. A.: Understanding and improving global crop response to ozone pollution. The Plant Journal, 90(5), 886-897,  
764 ~~doi:10.1111/tpj.13298~~, <https://doi.org/10.1111/tpj.13298>, 2017.

765

766 Avnery, S., Mauzerall, D. L., Liu, J., and Horowitz, L. W.: Global Crop Yield Reductions due to Surface Ozone Exposure: 1.  
767 Year 2000 Crop Production Losses and Economic Damage, Atmos. Environ., 45, 2284–2296, [https://doi:  
768 .org/10.1016/j.atmosenv.2010.11.045](https://doi.org/10.1016/j.atmosenv.2010.11.045), 2011.

769

770 Aguilos, M., Hérault, B., Burban, B., Wagner, F., & Bonal, D.: What drives long-term variations in carbon flux and balance  
771 in a tropical rainforest in French Guiana?. Agricultural and forest meteorology, 253, 114-123, ~~doi:  
772 10.1016/j.agrformet.2018.02.009~~ <https://doi.org/10.1016/j.agrformet.2018.02.009>, 2018.

105

106

107

774 Amos, B., Arkebauer, T. J., ~~&and~~ Doran, J. W.: Soil surface fluxes of greenhouse gases in an irrigated maize-based  
 775 agroecosystem. Soil Science Society of America Journal, 69(2), 387-395, ~~doi: 10.2136/sssaj2005.0387\_~~  
 776 <https://doi.org/10.2136/sssaj2005.0387>, 2015.

777

778 Beck, H. E., McVicar, T.R., Vergopolan, N. Berg, A., Lutsko, N. J., Dufour, A., Zeng, Z., Jiang, X., van Dijk, A. I. J. M.,  
 779 and Miralles, D. G.: High-resolution (1 km) Köppen-Geiger maps for 1901–2099 based on constrained CMIP6 projections.  
 780 Sci Data 10, 724-, ~~doi: 10.1038/s41597-023-02549-6~~ <https://doi.org/10.1038/s41597-023-02549-6>, 2023.

781

782 Broberg, M. C., Feng, Z., Xin, Y., ~~&and~~ Pleijel, H.: Ozone effects on wheat grain quality—A summary. Environmental  
 783 Pollution, 197, 203-213. ~~doi: 10.1016/j.envpol.2014.12.009~~, <https://doi.org/10.1016/j.envpol.2014.12.009>, 2015

784

785 Büker, P., Feng, Z., Uddling, J., Briolat, A., Alonso, R., Braun, S., Elvira, S., Gerosa, G., Karlsson, P.E., Le Thiec, D. and  
 786 Marzuoli, R., 2015: New flux based dose–response relationships for ozone for European forest tree species. Environmental  
 787 Pollution, 206, pp.163-174. ~~doi: 10.1016/j.envpol.2015.06.033~~ <https://doi.org/10.1016/j.envpol.2015.06.033>, 2015.

788

789 Bukowiecki, N., Steinbacher, M., Henne, S., Nguyen, N.A., Nguyen, X.A., Hoang, A.L., Nguyen, D.L., Duong, H.L.,  
 790 Engling, G., Wehrle, G., Gysel-Beer, M. and Baltensperger, U.: Effect of Large-scale Biomass Burning on Aerosol Optical  
 791 Properties at the GAW Regional Station Pha Din, Vietnam. Aerosol Air Qual. Res. 19: 1172-1187. ~~doi:~~  
 792 ~~10.4209/aaqr.2018.11.0406~~, <https://doi.org/10.4209/aaqr.2018.11.0406>, 2019.

793

794 Clifton, O. E., Fiore, A. M., Munger, J. W., ~~&and~~ Wehr, R.: Spatiotemporal controls on observed daytime ozone deposition  
 795 velocity over northeastern US forests during summer. Journal of Geophysical Research: Atmospheres, 124(10), 5612-5628,  
 796 ~~https://doi: 10.1029/2018JD029073~~, <https://doi.org/10.1029/2018JD029073>, 2019.

797

798 Clifton, O. E., D. L. Lombardozzi, A. M. Fiore, F. Paulot, ~~&and~~ L. W. Horowitz: Stomatal conductance influences  
 799 interannual variability and long-term changes in regional cumulative plant uptake of ozone. Environmental Research Letters.  
 800 ~~doi: 10.1088/1748-9326/abc3f1~~ <https://doi.org/10.1088/1748-9326/abc3f1>, 2020a.

801

802 Clifton, O. E., Paulot, F., Fiore, A. M., Horowitz, L. W., Correa, G., Baublitz, C. B., ... ~~&and~~ Weng, E.: Influence of  
 803 dynamic ozone dry deposition on ozone pollution. Journal of Geophysical Research: Atmospheres, 125(8),  
 804 ~~https://doi.org/doi: 10.1029/2020JD032398~~, 2020b.

108

109

110

805

806 Clifton, O. E., Schwede, D., Hogrefe, C., Bash, J. O., Bland, S., Cheung, P., Coyle, M., Emberson, L., Flemming, J., Fredj,  
807 E., Galmarini, S., Ganzeveld, L., Gazetas, O., Goded, I., Holmes, C. D., Horváth, L., Huijnen, V., Li, Q., Makar, P. A.,  
808 Mammarella, I., Manca, G., Munger, J. W., Pérez-Camanyo, J. L., Pleim, J., Ran, L., San Jose, R., Silva, S. J., Staebler, R.,  
809 Sun, S., Tai, A. P. K., Tas, E., Vesala, T., Weidinger, T., Wu, Z., and Zhang, L.: A single-point modeling approach for the  
810 intercomparison and evaluation of ozone dry deposition across chemical transport models (Activity 2 of AQMEII4), *Atmos.*  
811 *Chem. Phys.*, 23, 9911–9961, <https://doi.org/10.5194/acp-23-9911-2023>, 2023.

812

813 Chen, X., Quéléver, L. L. J., Fung, P. L., Kesti, J., Rissanen, M. P., Bäck, J., Keronen, P., Junninen, H., Petäjä, T.,  
814 Kerminen, V.-M., and Kulmala, M.: Observations of ozone depletion events in a Finnish boreal forest, *Atmos. Chem. Phys.*,  
815 18, 49–63, [doi: 10.5194/acp-18-49-2018](https://doi.org/10.5194/acp-18-49-2018), <https://doi.org/10.5194/acp-18-49-2018>, 2018 .

816

817 Copernicus Climate Change Service (C3S) (2017): ERA5: Fifth generation of ECMWF atmospheric reanalyses of the global  
818 climate. Copernicus Climate Change Service Climate Data Store (CDS), date of access: 27.11.2024.-  
819 <https://cds.climate.copernicus.eu/cdsapp#!/home> <https://cds.climate.copernicus.eu/cdsapp#!/home>

820

821 De Marco, A., Anav, A., Sicard, P., Feng, Z., ~~&and~~ Paoletti, E. ~~(2020)~~: High spatial resolution ozone risk-assessment for  
822 Asian forests. *Environmental Research Letters*, 15(10), 104095, [doi: 10.1088/1748-9326/abb501](https://doi.org/10.1088/1748-9326/abb501) [https://doi.org](https://doi.org/10.1088/1748-9326/abb501)  
823 [/10.1088/1748-9326/abb501](https://doi.org/10.1088/1748-9326/abb501), 2020.

824

825 Ducker, J. A., Holmes, C. D., Keenan, T. F., Fares, S., Goldstein, A. H., Mammarella, I., Munger, J. W., ~~&~~ and Schnell, J.:  
826 Synthetic ozone deposition and stomatal uptake at flux tower sites. *Biogeosciences*, 15(17), 5395–5413, [doi:10.5194/bg-15-](https://doi.org/10.5194/bg-15-5395-2018)  
827 [5395-2018](https://doi.org/10.5194/bg-15-5395-2018) <https://doi.org/10.5194/bg-15-5395-2018>, 2018.

828

829 Emberson, L.: Effects of ozone on agriculture, forests and grasslands. *Philosophical Transactions of the Royal Society A*,  
830 378(2183), 20190327, [doi: 10.1098/rsta.2019.0327](https://doi.org/10.1098/rsta.2019.0327) <https://doi.org/10.1098/rsta.2019.0327>, 2020.

831

832 Emmerichs, T.; Kerkweg, A.; Ouwersloot, H.; Fares, S.; Mammarella, I.; Taraborrelli, D.: A Revised Dry Deposition  
833 Scheme for Land–Atmosphere Exchange of Trace Gases in ECHAM/MESSy v2.54. *Geoscientific Model Development*, 14  
834 (1), 495–519. [doi: 10.5194/gmd-14-495-2021](https://doi.org/10.5194/gmd-14-495-2021) <https://doi.org/10.5194/gmd-14-495-2021>, 2021.

835

111  
112  
113

836 | Fares, S., Mereu, S., Scarascia Mugnozza, G., Vitale, M., Manes, F., Frattoni, M., ... [&and](#) Loreto, F.: The ACCENT-  
837 | VOCBAS field campaign on biosphere-atmosphere interactions in a Mediterranean ecosystem of Castelporziano (Rome):  
838 | site characteristics, climatic and meteorological conditions, and eco-physiology of vegetation. *Biogeosciences*, 6(6), 1043-  
839 | 1058, [doi: 10.5194/bg-6-1043-2009](#) <https://doi.org/10.5194/bg-6-1043-2009>, 2009.

840 |

841 | Fares, S. Measured and modelled stomatal and non-stomatal ozone fluxes in a mixed Mediterranean forest. In 25th ICP-  
842 | Vegetation Task Force Meeting. gennaio–2 febbraio 2012, Brescia, Italia.,2012.

843 |

844 | Fares, S., Savi, F., Muller, J., Matteucci, G., [&and](#) Paoletti, E.: Simultaneous measurements of above and below canopy  
845 | ozone fluxes help partitioning ozone deposition between its various sinks in a Mediterranean Oak Forest. *Agricultural and*  
846 | *Forest Meteorology*, 198, 181-191. <https://doi.org/10.1016/j.agrformet.2014.08.014>, 2014.

847 |

848 | Fares, S., Matteucci, G., Mugnozza, G. S., Morani, A., Calfapietra, C., Salvatori, E., ... [&and](#) Loreto, F.: Testing of models  
849 | of stomatal ozone fluxes with field measurements in a mixed Mediterranean forest. *Atmospheric environment*, 67, 242-251,  
850 | [doi: 10.1016/j.atmosenv.2012.11.007](#) <https://doi.org/10.1016/j.atmosenv.2012.11.007>, 2013.

851 |

852 | Feng, Z., Tang, H., Uddling, J., Pleijel, H., Kobayashi, K., Zhu, J., ... [&and](#) Guo, W.: A stomatal ozone flux–response  
853 | relationship to assess ozone-induced yield loss of winter wheat in subtropical China. *Environmental pollution*, 164, 16-23.  
854 | [doi: 10.1016/j.envpol.2012.01.014](#), 2012.

855 |

856 | <https://doi.org/10.1016/j.envpol.2012.01.014>, 2012.

857 |

858 | Fowler, D., Flechard, C., Cape, J.N. et al.: Measurements of Ozone Deposition to Vegetation Quantifying the Flux, the  
859 | Stomatal and Non-Stomatal Components. *Water, Air, & Soil Pollution* 130, 63–74. [doi: 10.1023/A:1012243317471](#)  
860 | <https://doi.org/10.1023/A:1012243317471>, 2001.

861 |

862 | Fuhrer, J., Val Martin, M., Mills, G., Heald, C. L., Harmens, H., Hayes, F., ... [&and](#) Ashmore, M. R.: Current and future  
863 | ozone risks to global terrestrial biodiversity and ecosystem processes. *Ecology and evolution*, 6(24), 8785-8799. <https://doi.org/10.1002/ece3.2568>, 2016.

864 |

865 |

866 Ganzeveld, L., & Lelieveld, J.: Dry deposition parameterization in a chemistry general circulation model and its influence  
867 on the distribution of reactive trace gases. *Journal of Geophysical Research: Atmospheres*, 100(D10), 20999-21012.  
868 <https://doi.org/10.1029/95JD02266>, 1995.

869

870 Gerosa, G., Vitale, M., Finco, A., Manes, F., Denti, A. B., & Cieslik, S. (2005): Ozone uptake by an evergreen  
871 Mediterranean Forest (*Quercus ilex*) in Italy. Part I: Micrometeorological flux measurements and flux partitioning.  
872 *Atmospheric Environment*, 39(18), 3255-3266, <https://doi.org/10.1016/j.atmosenv.2005.01.056>, 2005.

873

874 Gerosa, G., Marzuoli, R., Monteleone, B., Chiesa, M., & Finco, A.: Vertical ozone gradients above forests. Comparison  
875 of different calculation options with direct ozone measurements above a mature forest and consequences for ozone risk  
876 assessment. *Forests*, 8(9), 337. <https://doi.org/10.3390/f8090337>, 2017.

877 Gerosa G., Marzuoli R., Finco A.: Interannual variability of ozone fluxes in a broadleaf deciduous forest in Italy.  
878 *ELEMENTA: Science of the Anthropocene* 10(1), 00105. doi: 10.1525/elementa.2021.00105 [https://doi.org/](https://doi.org/10.1525/elementa.2021.00105)  
879 [/10.1525/elementa.2021.00105](https://doi.org/10.1525/elementa.2021.00105), 2022.

880 Guaita P.R., Marzuoli R., Gerosa G.A.: A regional scale flux-based O<sub>3</sub> risk assessment for winter wheat in northern Italy,  
881 and effects of different spatio-temporal resolutions. *Environmental Pollution* 333, 121860, [https://doi.org/](https://doi.org/10.1016/j.envpol.2023.121860)  
882 [10.1016/j.envpol.2023.121860](https://doi.org/10.1016/j.envpol.2023.121860), 2023.

883 Hardacre, C., Wild, O., and Emberson, L.: An evaluation of ozone dry deposition in global scale chemistry climate models,  
884 *Atmos. Chem. Phys.*, 15, 6419–6436, <https://doi.org/10.5194/acp-15-6419-2015>, 2015.

885 Hayes, F., Mills, G., Alonso, R., González-Fernández, I., Coyle, M., Grünhage, L., ... & Marzuoli, R.: A site-specific  
886 analysis of the implications of a changing ozone profile and climate for stomatal ozone fluxes in Europe. *Water, Air, & Soil*  
887 *Pollution*, 230, 1-15, <https://doi.org/10.1007/s11270-018-4057-x>, 2019.

888 Henne, S., ~~W.~~ Junkermann, ~~J.-M.W.~~, Kariuki, J. ~~M.~~, Aseyo, ~~J.~~ and ~~J.~~ Klausen: ~~J.~~ Mount Kenya Global Atmosphere Watch  
889 Station (MKN): Installation and Meteorological Characterization. *J. Appl. Meteor. Climatol.*, 47, 2946–2962, [https://doi.org/](https://doi.org/10.1175/2008JAMC1834.1)  
890 [10.1175/2008JAMC1834.1](https://doi.org/10.1175/2008JAMC1834.1), 2008a.

891 Henne, S., Klausen, J., Junkermann, W., Kariuki, J. M., Aseyo, J. O., and Buchmann, B.: Representativeness and  
892 climatology of carbon monoxide and ozone at the global GAW station Mt. Kenya in equatorial Africa, *Atmos. Chem. Phys.*,  
893 8, 3119–3139, doi: 10.5194/acp-8-3119-2008, <https://doi.org/10.5194/acp-8-3119-2008>, 2008b.

894 Hersbach, H., Bell, B., Berrisford, P., Hirahara, S., Horányi, A., Muñoz-Sabater, J., ... ~~&and~~ Thépaut, J. N.: The ERA5  
895 global reanalysis. Quarterly Journal of the Royal Meteorological Society, 146(730), 1999-2049. ~~doi: 10.1002/qj.3803,~~  
896 <https://doi.org/10.1002/qj.3803>, 2020.

897 Horváth, L., Koncz, P., Möring, A. et al.: An Attempt to Partition Stomatal and Non-stomatal Ozone Deposition Parts on a  
898 Short Grassland. Boundary-Layer Meteorol 167, 303–326 ~~(2018),~~ <https://doi.org/10.1007/s10546-017-0310-x>, [2018](https://doi.org/10.1007/s10546-017-0310-x).

899 Huang, M., Crawford, J. H., Carmichael, G. R., Bowman, K. W., Kumar, S. V., and Sweeney, C.: Satellite soil moisture data  
900 assimilation impacts on modeling weather variables and ozone in the southeastern US – Part 2: Sensitivity to dry-deposition  
901 parameterizations, Atmos. Chem. Phys., 22, 7461–7487, <https://doi.org/10.5194/acp-22-7461-2022>, 2022.

902

903 Jägermeyr, J, Müller, C., Minoli, S., Ray, D., and Siebert., S.: GGCM Phase 3 crop calendar [Data set]. Zenodo. ~~doi:~~  
904 ~~10.5281/zenodo.5062513~~ <https://doi.org/10.5281/zenodo.5062513>, 2021a.

905

906 Jägermeyr et al.: Climate impacts on global agriculture emerge earlier in new generation of climate and crop, Nature Food,  
907 2, 873–885, <https://www.nature.com/articles/s43016-021-00400-y>, 2021b.

908

909 Junninen, H., Lauri, A., Keronen, P., Aalto, P., Hiltunen, V., Hari, P., Kulmala, M. 2009. Smart-SMEAR: online data  
910 exploration and visualization tool for SMEAR stations. Boreal Environment Research 14, 447–457,  
911 <http://www.borenv.net/BER/pdfs/ber14/ber14-447.pdf>, 2009.

912

913 Grulke, N. E., ~~& and~~ Heath, R. L. ~~(2020),~~ Ozone effects on plants in natural ecosystems. Plant Biology, 22, 12-37.  
914 <https://doi.org/10.1111/plb.12971>, [2020](https://doi.org/10.1111/plb.12971).

915

916 Khan, A. M., Clifton, O. E., Bash, J. O., Bland, S., Booth, N., Cheung, P., ... ~~&and~~ Stoy, P. C.: Ozone dry deposition  
917 through plant stomata: Multi-model comparison with flux observations and the role of water stress as part of AQMEII4  
918 Activity 2. EGU sphere, 2024, 1-34. ~~doi: 10.5194/egusphere-2024-3038,~~ <https://doi.org/10.5194/egusphere-2024-3038>,  
919 2024.

920

921 Kattge, J., ~~& and~~ Knorr, W.: Temperature acclimation in a biochemical model of photosynthesis: a reanalysis of data from  
922 36 species. Plant, cell & environment, 30(9), 1176-1190, <https://doi.org/10.1111/j.1365-3040.2007.01690.x>, 2007.

923

924 Krause, D., & Thörnig, P.: JURECA: modular supercomputer at Jülich supercomputing centre. Journal of large-scale  
 925 research facilities JLSRF, 4, A132-A132, [10.17815/jlsrf-4-121](https://doi.org/10.17815/jlsrf-4-121), <https://doi.org/10.17815/jlsrf-4-121>, 2018.

926

927 Li, M., Wu, P., & Ma, Z.: A comprehensive evaluation of soil moisture and soil temperature from third-generation  
 928 atmospheric and land reanalysis data sets. Int. J. Climatol, 40(13), 5744-5766, [doi: 10.1002/joc.6549](https://doi.org/10.1002/joc.6549) [https://doi.org](https://doi.org/10.1002/joc.6549)  
 929 [/10.1002/joc.6549](https://doi.org/10.1002/joc.6549), 2020.

930

931 Leung, F., Williams, K., Sitch, S., Tai, A. P., Wiltshire, A., Gornall, J., ... & Scoby, D.: Calibrating soybean parameters  
 932 in JULES 5.0 from the US-Ne2/3 FLUXNET sites and the SoyFACE-O<sub>3</sub> experiment. Geoscientific Model  
 933 Development, 13(12), 6201-6213, doi: 10.5194/gmd-13-6201-2020, 2020.

934

935 Mäkelä, J., Knauer, J., Aurela, M., Black, A., Heimann, M., Kobayashi, H., ... & Aalto, T.: Parameter calibration and  
 936 stomatal conductance formulation comparison for boreal forests with adaptive population importance sampler in the land  
 937 surface model JSBACH. Geoscientific Model Development, 12(9), 4075-4098. [https://doi.org/10.5194/gmd-12-4075-](https://doi.org/10.5194/gmd-12-4075-2019)  
 938 [2019](https://doi.org/10.5194/gmd-12-4075-2019)<https://doi.org/10.5194/gmd-12-4075-2019>, 2019.

939

940 McGrath, J. M., Betzelberger, A. M., Wang, S., Shook, E., Zhu, X. G., Long, S. P., & Ainsworth, E. A.: An analysis of  
 941 ozone damage to historical maize and soybean yields in the United States. Proceedings of the National Academy of Sciences,  
 942 112(46), 14390-14395. [doi: 10.1073/pnas.1509777112](https://doi.org/10.1073/pnas.1509777112), <https://doi.org/10.1073/pnas.1509777112>, 2015.

943

944 Meszaros, R., Horváth, L., Weidinger, T., Neftel, A., Nemitz, E., Dämmgen, U., ... & Loubet, B.: Measurement  
 945 and modelling ozone fluxes over a cut and fertilized grassland. Biogeosciences, 6(10), 1987-1999.  
 946 <https://doi.org/10.5194/bg-6-1987-2009>, 2009.

947

948 Meyers, T. P., Finkelstein, P., Clarke, J., Ellestad, T. G., & Sims, P. F.: A multilayer model for inferring dry  
 949 deposition using standard meteorological measurements. Journal of Geophysical Research: Atmospheres, 103(D17), 22645-  
 950 22661, <https://doi.org/10.1029/98JD01564>, 1998.

951

952 Mills, G., Hayes, F., Simpson, D., Emberson, L., Norris, D., Harmens, H. and Büker, P.: Evidence of widespread  
 953 effects of ozone on crops and (semi-)natural vegetation in Europe (1990–2006) in relation to AOT40- and flux-based risk  
 954 maps. Global Change Biology, 17: 592-613, <https://doi.org/10.1111/j.1365-2486.2010.02217.x>, 2011.

955



956 Mills, G., ~~Håkan~~Pleijel, ~~Christopher S.H.~~, Malley, ~~Baerbel~~C. S., Sinha, ~~Owen R.B.~~, Cooper, ~~Martin G.O. R.~~, Schultz,  
957 ~~Howard S.M. G.~~, Neufeld, ~~David H. S.~~, Simpson, ~~Katrina D.~~, Sharps, ~~Zhaozhong K.~~, Feng, ~~Giacomo Z.~~, Gerosa, ~~Harry G.~~,  
958 Harmens, ~~Kazuhiko H.~~, Kobayashi, ~~Pallavi K.~~, Saxena, ~~Elena P.~~, Paoletti, ~~Vinayak E.~~, Sinha, ~~Xiaobin V.~~, Xu, ~~X.~~: Tropospheric  
959 Ozone Assessment Report: Present-day tropospheric ozone distribution and trends relevant to vegetation. Elementa: Science  
960 of the Anthropocene ~~1 January 2018~~; 6 47, <https://doi.org/10.1525/elementa.302>, 2018.  
961  
962 Monks, P. S., Archibald, A. T., Colette, A., Cooper, O., Coyle, M., Derwent, R., ... ~~&and~~ Williams, M. L. ~~(2015).~~:  
963 Tropospheric ozone and its precursors from the urban to the global scale from air quality to short-lived climate forcer.  
964 Atmospheric chemistry and physics, 15(15), 8889-8973. <https://doi.org/10.5194/acp-15-8889-2015>, 2015.  
965  
966 Pastorello, G., Trotta, C., Canfora, E. ~~et al. (2020).~~: The FLUXNET2015 dataset and the ONEFlux processing pipeline for  
967 eddy covariance data. Sci Data 7, 225, <https://doi.org/10.1038/s41597-020-0534-3>, 2020.  
968  
969 Pieber, S.M., Henne, S., Nguyen, N.A., Nguyen, DL., Steinbacher, M. ~~(2023).~~: Trace Gases and Air Quality in  
970 Northwestern Vietnam During Recurrent Biomass Burning on the Indochina Peninsula Since 2014—Field Observations and  
971 Atmospheric Simulations. In: Vadrevu, K.P., Ohara, T., Justice, C. (eds) Vegetation Fires and Pollution in Asia. Springer,  
972 Cham. [https://doi.org/10.1007/978-3-031-29916-2\\_32](https://doi.org/10.1007/978-3-031-29916-2_32), 2023.  
973  
974 Pleim, J. and Ran, L., ~~2011.~~: Surface flux modeling for air quality applications. Atmosphere, 2(3), pp.271-302.  
975 <https://doi.org/10.3390/atmos2030271>, 2011.  
976  
977 Poyatos, R., Granda, V., Flo, V., Adams, M. A., Adorján, B., Aguadé, D., ... ~~&and~~ Van Der Tol, C. ~~(2020).~~: Global  
978 transpiration data from sap flow measurements: the SAPFLUXNET database. Earth System Science Data, 13, 2607–2649, <https://doi.org/10.5194/essd-13-2607-2021>, 2021.  
979  
980  
981 Putaud J.P., ~~P.~~Bergamaschi, ~~M.P.~~, Bressi, ~~F.M.~~, Cavalli, ~~A.F.~~, Cescatti, ~~D.A.~~, Daou, ~~A.D.~~, Dell’Acqua, ~~K.A.~~, Douglas,  
982 ~~M.K.~~, Duerr, ~~I.M.~~, Fumagalli, I., Goded, ~~F.L.~~, Grassi, ~~C.F.~~, Gruening, ~~J.C.~~, Hjorth, ~~N.R.J.~~, Jensen, ~~F.N. R.~~, Lagler, ~~G.F.~~,  
983 Manca, ~~S.G.~~, Martins Dos Santos, ~~M.S.~~, Matteucci, ~~R.M.~~, Passarella, ~~V.R.~~, Pedroni, ~~O.V.~~, Pokorska, ~~D.O.~~, Roux, ~~D.~~: JRC  
984 – Ispra Atmosphere - Biosphere - Climate Integrated monitoring Station: 2014 Report; EUR 27639 EN, <https://doi.org/10.2788/570407>, 2014.  
985  
986

987 | Ran, L., Pleim, J., Song, C., Band, L., Walker, J.T. and Binkowski, F.S.,~~(2017).~~ A photosynthesis-based two-leaf canopy  
988 | stomatal conductance model for meteorology and air quality modeling with WRF/CMAQ PX LSM. Journal of Geophysical  
989 | Research: Atmospheres, 122(3), pp.1930-1952, <https://doi.org/10.1002/2016JD025583>, ~~2017~~.  
990 |  
991 | Raghav, P., Kumar, M., ~~&and~~ Liu, Y.,~~(2023).~~ Structural constraints in current stomatal conductance models preclude  
992 | accurate estimation of evapotranspiration and its partitions, <https://doi.org/10.1029/2024WR037652>, ~~2023~~.  
993 |  
994 | Ramya, A., Dhevagi, P., Poornima, R., Avudainayagam, S., Watanabe, M., ~~&and~~ Agathokleous, E.,~~(2023).~~ Effect of ozone  
995 | stress on crop productivity: A threat to food security. *Environmental Research*, 116816.  
996 | <https://doi.org/10.1016/j.envres.2023.116816>~~https://doi.org/10.1016/j.envres.2023.116816~~, ~~2023~~.  
997 |  
998 | Savi, F. and Fares, S.,~~(2014).~~ Ozone dynamics in a Mediterranean Holm oak forest: comparison among transition periods  
999 | characterized by different amounts of precipitation. *Annals of Silvicultural Research* 38(1) 1-6  
1000 | <http://dx.doi.org/10.12899/ASR-801>, ~~2014~~  
1001 |  
1002 | Schröder, S., Schultz, M. G., Selke, N., Sun, J., Ahring, J., Mozaffari, A., Romberg, M., Epp, E., Lensing, M.,  
1003 | Apweiler, S., Leufen, L. H., Betancourt, C., Hagemeier, B., Rajveer, S.,~~(2021).~~ TOAR Data Infrastructure,  
1004 | <https://doi.org/10.34730/4d9a287dec0b42f1aa6d244de8f19eb3>, ~~2021~~.  
1005 |  
1006 | Schucht, S., Tognet, F., Létinois, L. and Ineris, I.N.,~~2021.~~ Wheat yield loss in 2019 in Europe due to ozone exposure.,  
1007 | Eionet Report-ETC/ATNI, ~~2021~~.  
1008 |  
1009 | Silva, S. J.,~~&and~~ Heald, C. L.,~~(2018).~~ Investigating dry deposition of ozone to vegetation. Journal of Geophysical  
1010 | Research: Atmospheres, 123(1), 559-573. <https://doi.org/10.1002/2017JD027278>, ~~2018~~.  
1011 |  
1012 | Stella, Patrick, et al.,~~-. Predicting and partitioning ozone fluxes to maize crops from sowing to harvest: the Surf atm-O 3~~  
1013 | ~~model-. Biogeosciences 8.10-(2011)-, 2869-2886. https://doi.org/10.5194/bg-8-2869-2011https://doi.org/10.5194/bg-8-~~  
1014 | ~~2869-2011, 2011.~~  
1015 |  
1016 | Stella, P., Personne, E., Lamaud, E., Loubet, B., Trebs, I., & Cellier, P. (2013). Assessment of the total, stomatal, cuticular,  
1017 | and soil 2 year ozone budgets of an agricultural field with winter wheat and maize crops-. Journal of Geophysical Research:  
1018 | Biogeosciences, 118(3), 1120-1132, <https://doi.org/10.1002/jgrg.20094>-, ~~2013~~.  
1019 |

1020 Sofen, E. D., Bowdalo, D., Evans, M. J., Apadula, F., Bonasoni, P., Cupeiro, M., ... ~~&and~~ Tørseth, K. ~~(2016).~~ Gridded  
1021 global surface ozone metrics for atmospheric chemistry model evaluation. *Earth System Science Data*, 8(1), 41-59.  
1022 <https://doi.org/10.5194/essd-8-41-2016>, <https://doi.org/10.5194/essd-8-41-2016>, 2016.

1023

1024 Sun, S., Tai, A. P. K., Yung, D. H. Y., Wong, A. Y. H., Ducker, J. A., and Holmes, C. D.: Influence of plant ecophysiology  
1025 on ozone dry deposition: comparing between multiplicative and photosynthesis-based dry deposition schemes and their  
1026 responses to rising CO<sub>2</sub> level, *Biogeosciences*, 19, 1753–1776, <https://doi.org/10.5194/bg-19-1753-2022>, 2022.

1027

1028 Tai, A. P., Yung, D. H., & Lam, T. ~~(2024).~~ Terrestrial Ecosystem Model in R (TEMIR) version 1.0: simulating  
1029 ecophysiological responses of vegetation to atmospheric chemical and meteorological changes. *Geoscientific Model*  
1030 *Development*, 17(9), 3733-3764, <https://doi.org/10.5194/gmd-17-3733-2024>, 2024.

1031

1032 Travis, K. R., ~~& and~~ Jacob, D. J. ~~(2019).~~ Systematic bias in evaluating chemical transport models with maximum daily 8 h  
1033 average (MDA8) surface ozone for air quality applications: a case study with GEOS-Chem v9. 02. *Geoscientific Model*  
1034 *Development*, 12(8), 3641-3648. <https://doi.org/10.5194/gmd-12-3641-2019><https://doi.org/10.5194/gmd-12-3641-2019>,  
1035 [2019](https://doi.org/10.5194/gmd-12-3641-2019).

1036

1037 UNECE LRTAP (2017). III. Mapping critical levels for vegetation. Available at:  
1038 [https://icpvegetation.ceh.ac.uk/sites/default/files/FinalnewChapter3v4Oct2017\\_000.pdf](https://icpvegetation.ceh.ac.uk/sites/default/files/FinalnewChapter3v4Oct2017_000.pdf)

1039 Visser, A. J., Ganzeveld, L. N., Goded, I., Krol, M. C., Mammarella, I., Manca, G., and Boersma, K. F. ~~(2021).~~ Ozone  
1040 deposition impact assessments for forest canopies require accurate ozone flux partitioning on diurnal timescales, *Atmos.*  
1041 *Chem. Phys.*, 21, 18393–18411, <https://doi.org/10.5194/acp-21-18393-2021>, 2021.

1042

1043 Walker, A. P., Quaife, T., Van Bodegom, P. M., De Kauwe, M. G., Keenan, T. F., Joiner, J., ... & Woodward, F. I. ~~(2017).~~  
1044 The impact of alternative trait-scaling hypotheses for the maximum photosynthetic carboxylation rate ( $V_{Cmax}$ ) on global gross  
1045 primary production. *New Phytologist*, 215(4), 1370-1386, <https://doi.org/10.1111/nph.14623>, 2017:

1046

1047 Wang, T., Wang, F., Song, H., Zhou, S., Ru, X. and Zhang, H., 2022. Maize yield reduction and economic losses caused by  
1048 ground-level ozone pollution with exposure-and flux-response relationships in the North China Plain. *Journal of*  
1049 *Environmental Management*, 324, p.116379. <https://doi.org/10.1016/j.jenvman.2022.116379>[https://doi.org/10.1016/](https://doi.org/10.1016/j.jenvman.2022.116379)  
1050 [j.jenvman.2022.116379](https://doi.org/10.1016/j.jenvman.2022.116379), 2022.

1051

1052 | Wilkinson, M. D., Dumontier, M., Aalbersberg, I. J., Appleton, G., Axton, M., Baak, A., ... & Mons, B.-(2016).: The FAIR  
 1053 Guiding Principles for scientific data management and stewardship. Scientific data, 3(1), 1-9.  
 1054 | <https://doi.org/10.1038/sdata.2016.18>, 2016.  
 1055  
 1056 | Wong, A. Y. H., Geddes, J. A., Ducker, J. A., Holmes, C. D., Fares, S., Goldstein, A. H., et al.-(2022).: New evidence for  
 1057 the importance of non-stomatal pathways in ozone deposition during extreme heat and dry anomalies. Geophysical  
 1058 ResearchLetters, 49, e2021GL095717, <https://doi.org/10.1029/2021GL095717><https://doi.org/10.1029/2021GL095717>, 2022.  
 1059  
 1060 | Yen M-Ch. , Peng C-M., Chen T.-C., Chen Ch.-S., Lin N.-H., Tzeng R.-Y., Lee Y.-A. , Lin Ch.-Ch.-(2013).: Climate and  
 1061 weather characteristics in association with the active fires in northern Southeast Asia and spring air pollution in Taiwan  
 1062 during 2010 7-SEAS/Dongsha Experiment, Atmospheric Environment, Volume 78, Pages 35-50, ISSN-1352-2310,m-  
 1063 <https://doi.org/10.1016/j.atmosenv.2012.11.015>-, 2013.  
 1064  
 1065 | Young, P. J.; Naik, V.; Fiore, A. M.; Gaudel, A.; Guo, J.; Lin, M.; Neu, J.; Parrish, D.; Rieder, H.;Schnell, J. others.:  
 1066 Tropospheric Ozone Assessment Report: Assessment of Global-Scale Model Performance for Global and Regional Ozone  
 1067 Distributions, Variability, and Trends. Elem Sci Anth, 6 (1), [doi:10.1525/elementa.265](https://doi.org/10.1525/elementa.265) <https://doi.org/10.1525/elementa.265>,  
 1068 2018.  
 1069  
 1070 | Zhang, L., Brook, J. R., and Vet, R.: A revised parameterization for gaseous dry deposition in air-quality models, Atmos.  
 1071 Chem. Phys., 3, 2067–2082, [doi:10.5194/acp-3-2067-2003](https://doi.org/10.5194/acp-3-2067-2003) <https://doi.org/10.5194/acp-3-2067-2003>, 2003.  
 1072  
 1073 | Zhang, W., Feng, Z., Wang, X., Liu, X., & Hu, E.: Quantification of ozone exposure-and stomatal uptake-yield response  
 1074 relationships for soybean in Northeast China. Science of the Total Environment, 599, 710-720.-[doi:](https://doi.org/10.1016/j.scitotenv.2017.04.231)  
 1075 [10.1016/j.scitotenv.2017.04.231](https://doi.org/10.1016/j.scitotenv.2017.04.231), 2017., <https://doi.org/10.1016/j.scitotenv.2017.04.231>, 2017.

1082  
1083  
1084  
1085

1086

1087   **Appendix**

1088   Table A1: Abbreviations

Symbol	Long name
rsmin	Minimum stomatal resistance in [s m <sup>-1</sup> ]
gsmax	Maximum stomatal conductance in [m s <sup>-1</sup> ]
RH	Relative humidity in [%]
LAI	Leaf area index in [m <sup>2</sup> m <sup>-2</sup> ]
sd, sn	snow depth in [m] and snow cover
ssrd, strd	solar and thermal flux at surface in [W m <sup>-2</sup> ]
sw	Soil wetness [m]
al_vis:	albedo (visible)
cwv	canopy water content in [kg m <sup>-2</sup> ]
SWC	Soil water content
SM	Soil moisture [m <sup>3</sup> m <sup>-3</sup> ]
wdir	geo wind direction [°]
wspeed	Wind speed in [ <del>msm</del> s <sup>-1</sup> ]
cv	Vegetation fraction [m <sup>2</sup> m <sup>-2</sup> ]
P	Precipitation in [mm]
P_rate	Precipitation rate in [mm h <sup>-1</sup> ], [kg m <sup>-2</sup> s <sup>-1</sup> ], [m s <sup>-1</sup> ]
Tair, Tsoil, T2m	Air, soil, 2m temperature in [K]
VPD	Vapour pressure deficit [kPa]
Pa	Air pressure [hPa]
Rn, Gr	Net and global radiation [W m <sup>-2</sup> ]
u*	Friction velocity [m s <sup>-1</sup> ]

138  
139  
140

O <sub>3</sub> , CO <sub>2</sub>	O <sub>3</sub> and CO <sub>2</sub> concentration in [ppb] und [ppt]
h_dis, z0	Displacement height [m], roughness length [m]
CF	Cloud fraction
LUC	Land usage category

1089

1090

